Chapter 5: Microstructure and strengthening mechanisms in nickel added low-density duplex steel

5.1 Introduction

An austenitic low-density duplex steel (Fe-18Mn-10Al-1C-6Ni) (P3) is produced using vacuum induction melting, followed by hot rolling and quenching in water (PD3). The PD3 samples are annealed (930°C for 30 min) and water quenched (PD3-A) to felicitate B2 formation. Later aging treatments are performed to get kappa carbide precipitation for different time periods. The microstructure and mechanical properties of PD3, PD3-A and PD3-AB_{30} (Peak age hardened sample) samples are reported in the Chapter 5.

5.2 Results

5.2.1 Phase diagram and Phases

The calculated phase diagram (Figure 5.1(a)) for Fe-18 mass % Mn-1 mass% C-6 mass % Ni-10.5 mass % Al predicts the formation majority of disorder δ ferrite (BCC_A2) and liquid at 1366°C. On slow cooling, austenite formation takes place at 1264 °C. Liquid disappears completely at 1248°C. At 1242°C, ordering of BCC_A2 takes place and completely converts to order B2 (BCC_B2) at 1222°C. Below 890°C, FCC_A1 decomposes to kappa carbide and ordered B2. At 613°C, FCC_A1 partially decomposes to kappa carbide and disordered α ferrite. Below 526°C, FCC_A1 is partially decomposing to ordered B2-2 and disorder α ferrite A2. Below 455°C austenite completely decomposes to kappa carbide and disorder α ferrite. Therefore, under equilibrium cooling conditions phase diagram predicts that at room temperature stable phases are 63.3% disorder α ferrite, 21.9% order B2, and the remaining kappa carbide. However, on casting in a copper mold, due to

rapid cooling, X-ray diffraction patterns revealed 84 % austenite and 16% δ ferrite at room temperature (Figure 5.1(b)).

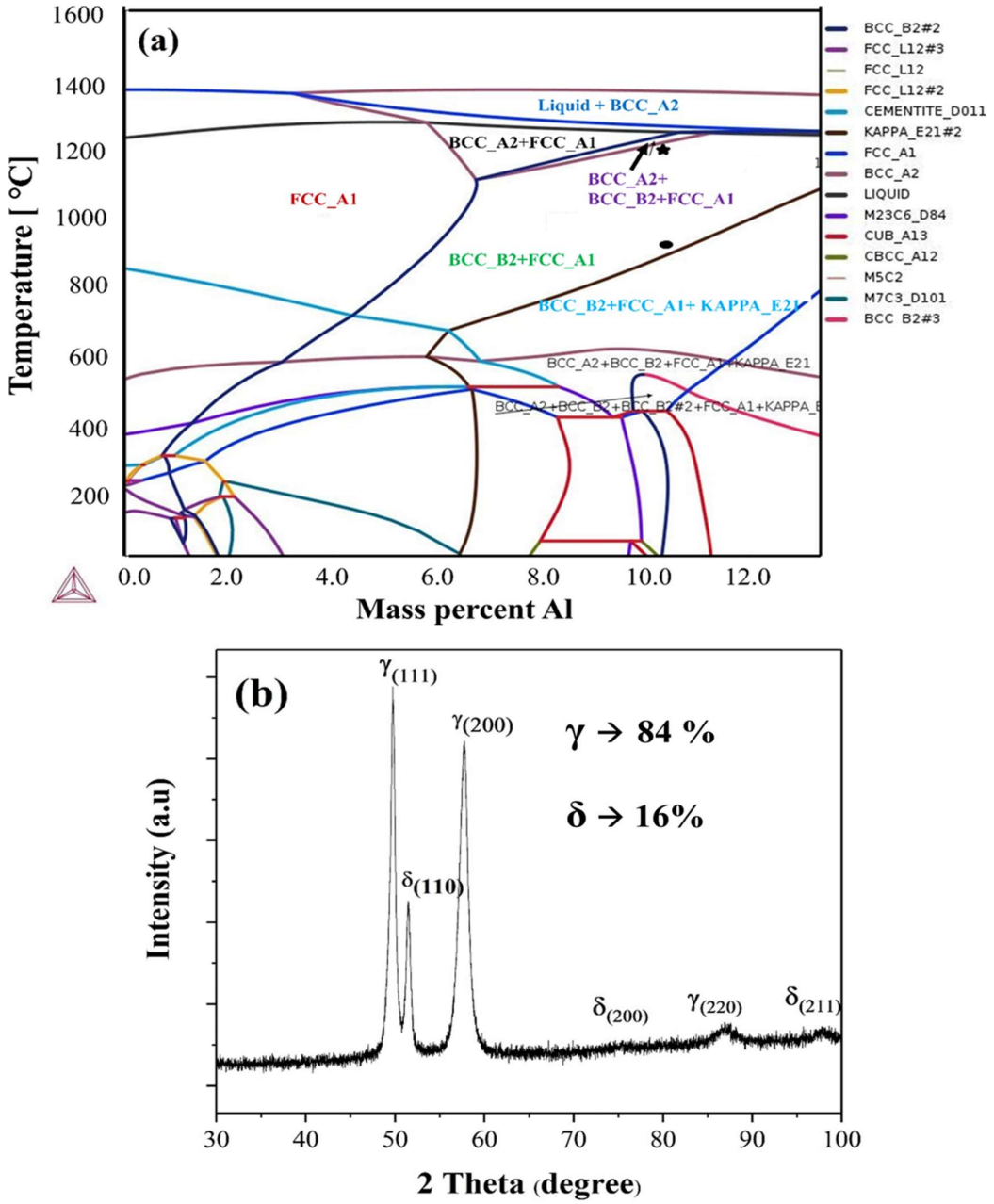

Figure 5.1: (a) Calculated phase diagram of Fe-18Mn-XAl-1C-6Ni alloy system using Thermo-246 Calc (version 2022a) (The star mark indicates the homogenization temperature and oval mark indicates the annealing temperature), and (b) XRD pattern of the cast alloy.

5.2.2 Optical microstructure

Microstructure of as cast P3 consists of dendritic austenite and δ ferrite (Figure 5.2(a)). On homogenization of the cast material at 1200°C followed by hot rolling 1150°C-950°C, dendritic δ ferrite is broken and get ordered to B2. During hot rolling B2 is elongated to banded B2 of size of 95 ± 21 μm in length and 3.1 ± 1.1 μm width, with additional precipitation of globular B2 of size of 0.9 ± 0.2 μm within austenite and at austenite grain boundaries (Figure 5.2(b)). The dendritic structure of austenite is also broken and becomes equiaxed with an average grain size of 5.7 ± 1.3 μm. Annealing twins are developed within dynamically recrystallized austenite grains. As deformation continued below 1000°C, some austenite grains are elongated, and a few deformation bands are also observed within deformed austenite (Figure 5.2(b)).

The microstructure of homogenized, hot rolled and water quenched followed by annealed at 930°C for 30 min and water quenched low density steel (PD3-A) displays the majority of austenite grains in equiaxed form with some amount of non-recrystallized one (Figure 5.3(a), (b)). On annealing, fine B2 platelets gets precipitated within the matrix, and coarse B2 platelets precipitated at deformation bands. The average size of austenite is 8.3 ± 5 μm. The average size of B2 platelets is observed with a width of 0.21 ± 0.08 μm, and a length of 0.79 ± 0.25 μm (Figure 5.3 (b)). Globular B2 precipitates gets coarsen to average diameter of 1.40 ± 0.6 μm (Figures 5.3 (a), (b)) upon annealing.

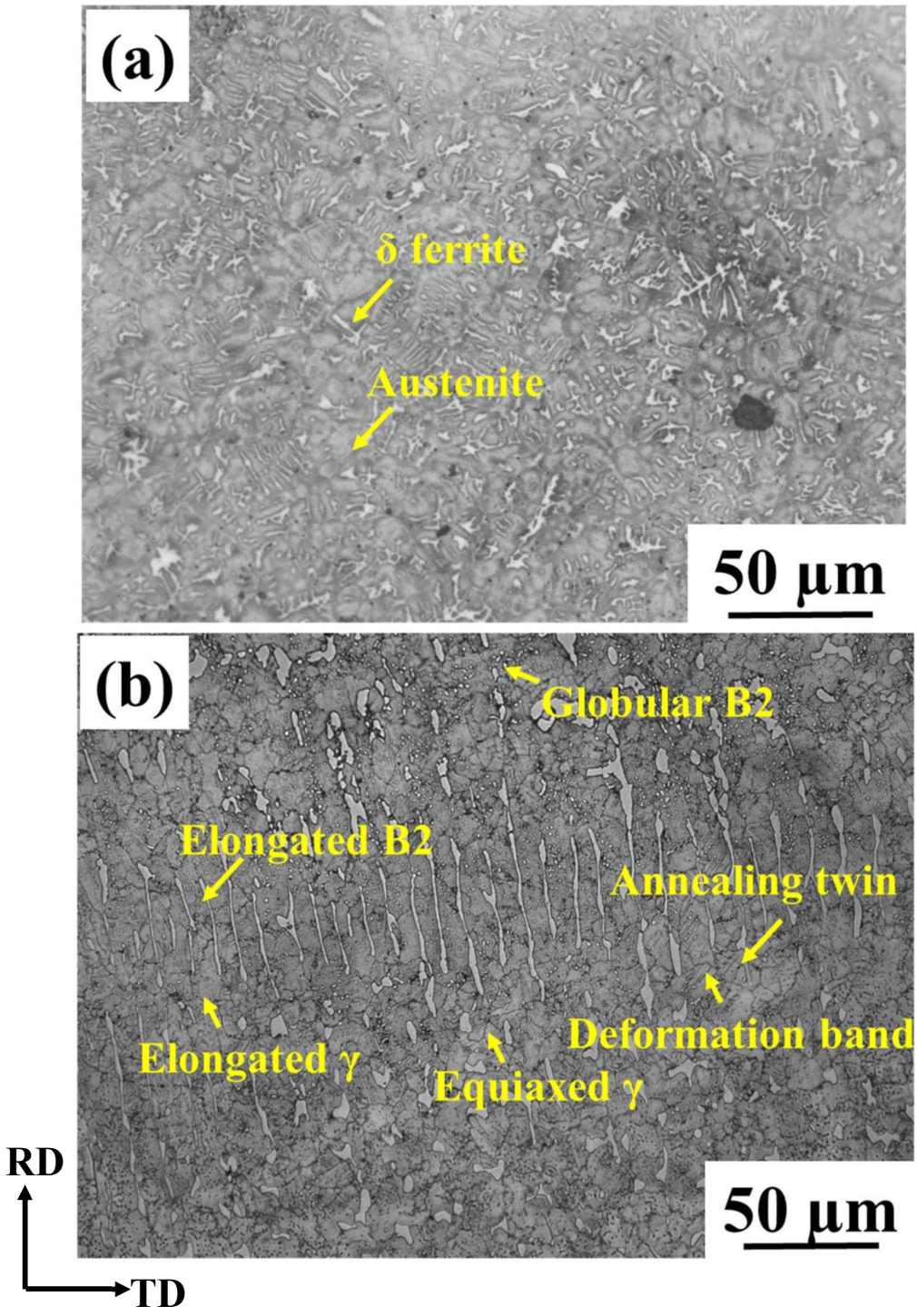

Figure 5.2: Optical micrographs of steel of selected composition in (a) as-cast condition and (b) homogenized at 1200°C followed by hot rolling and water quenching (PD3). RD and TD indicate rolling and transverse directions, respectively.

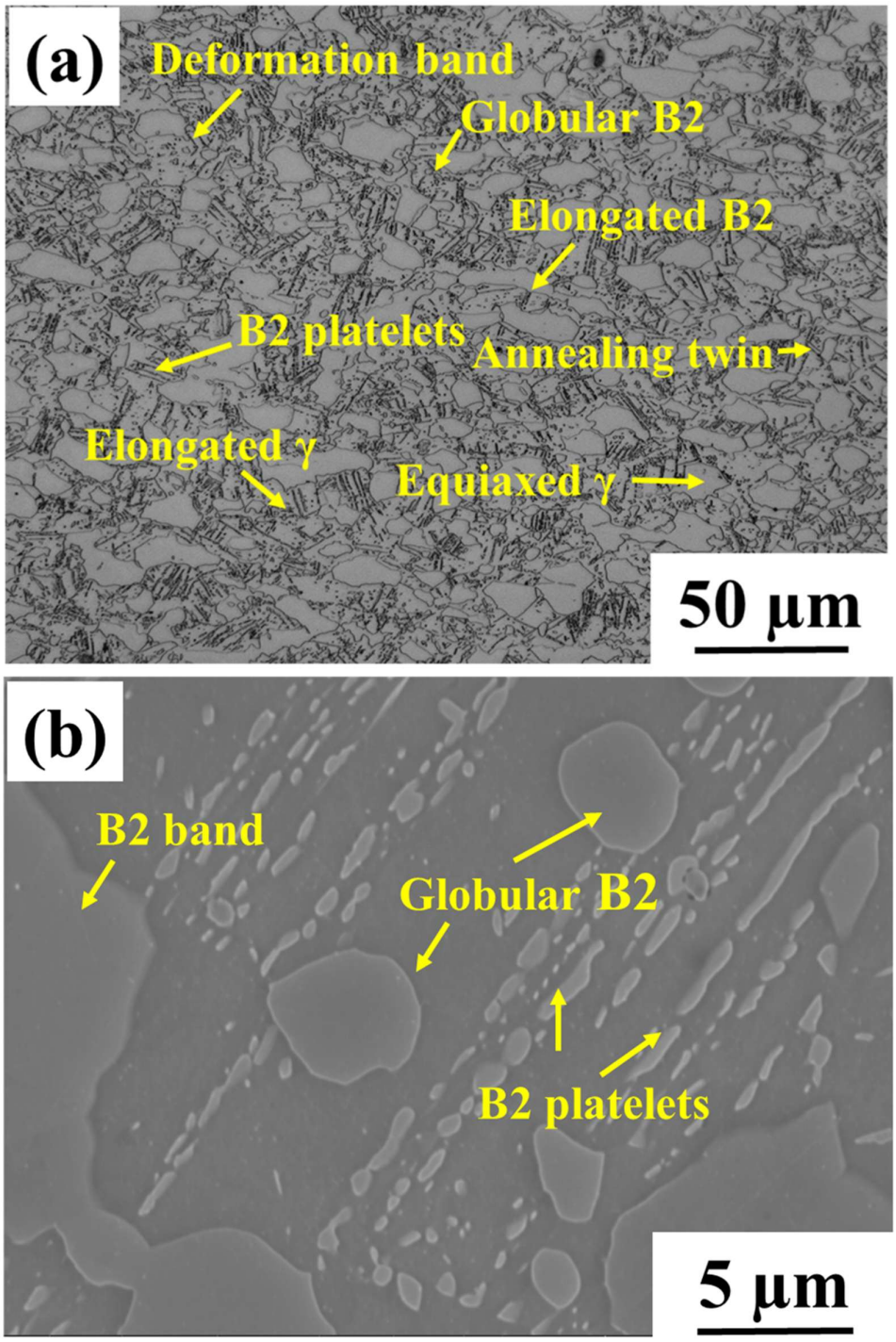

Figure 5.3: Low-density steel after annealing of PD3 sample, at 930°C for 30 min followed by water quenching (PD3-A), (a) optical micrograph (b) SEM-secondary electron micrograph revealing different morphologies of B2 phase. The arrow indicates the respective precipitates.

5.2.3 Phase analysis, size of crystal and crystalline defects

X-Ray Diffraction (XRD) pattern analysis of PD3 reveals the presence of 87% austenite and 13% of ordered B2 (Figure 5.4). The crystallite sizes of austenite and B2 phase are 42 nm and 39 nm, respectively (Table 5.1). The respective residual micro-strains in austenite and B2 are 0.26% and 0.27%. Dislocation densities in austenite and B2 are calculated to be $8.3 \times 10^{14}/m^2$ and $10.1 \times 10^{14}/m^2$, respectively. PD3-A reports the presence of austenite and B2 in the proportions of 82 % and 18 % (Figure 5.4). The crystallite sizes of austenite and B2 phase are 73 nm and 53 nm, respectively. The respective residual micro strains in austenite and B2 are 0.16 % and 0.20 %. Dislocation densities in austenite and B2 are estimated to be $2.9 \times 10^{14}/m^2$ and $5.4 \times 10^{14}/m^2$, respectively. PD3-A samples are aged at 550°C. Vickers hardness value increases with increasing aging time, reaches a maximum value at 30 min and thereafter, it decreases (Table 5.2).

XRD pattern of the peak-aged material (designated as PD3-AB_{30}) display intense peaks of austenite and B2 phases (Figure 5.4). The crystallite sizes of austenite and B2 phase are 74 nm and 54 nm, respectively (Table 5.1). The respective residual micro strains in austenite and B2 are 0.18 and 0.21%. Dislocation densities in austenite and B2 are estimated to be $3.8 \times 10^{14}/m^2$ and $5.6 \times 10^{14}/m^2$, respectively. The areal fraction analysis of the peaks reveals the material contains about 71 vol % austenite, 21 vol% percent of B2, and kappa carbide of 3 vol% and α- ferrite of 5% approximately.

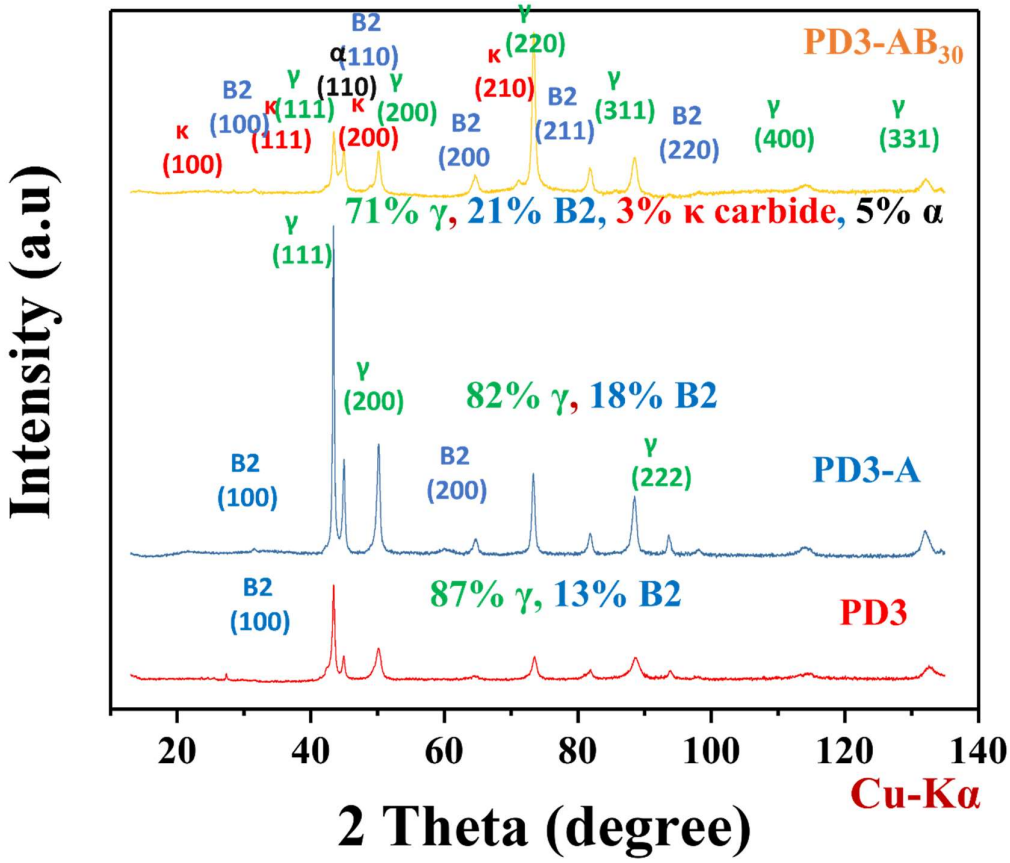

Figure 5.4: (a) X-ray diffraction patterns of PD3, PD3-A, and PD3-AB_{30} samples.

Table 5.1: Crystallite size, micro strain, and dislocation densities of austenite and B2 phases in PD3, PD3-A, and PD3-AB_{30} samples.

Sample	Lattice parameter of austenite (Å)	Crystallite size (nm)		Micro strain (%)		Dislocation density (10^{14} /m^2)	
		Austenite	B2	Austenite	B2	Austenite	B2
PD3	3.676	42	39	0.26	0.27	8.3	10.1
PD3-A	3.681	73	53	0.16	0.20	2.9	5.4
PD3-AB_{30}	3.684	74	54	0.18	0.21	3.8	5.6

Table 5.2: Vickers hardness of PD3-A samples aged at 550°C.

Ageing time (min)	Hardness (HV)
0	372 ± 9
10	408 ± 11
20	440 ± 18
30	480 ± 7
40	434 ± 8
50	421 ± 13
60	412 ± 4

Compositions of microstructural features are estimated by EDS (by mass %) without carbon analysis. The typical composition of austenite in PD3 is Fe-19.06 Mn-9.52 Al-4.53 Ni. Compositions of elongated and globular B2 in PD3 are reported to be Fe-12.71 Mn-15.83 Al-14.49 Ni and Fe-14.09 Mn-15.13 Al-12.25 Ni (Table 5.3). On annealing at 930°C, in PD3-A compositions of austenite and elongated B2 are Fe-19.50 Mn-9.40 Al-4.01 Ni and Fe-11.58 Mn-16.74 Al-15.55 Ni, respectively (Table 5.3). On the other hand, the globular B2 has compositions of Fe-13.87 Mn-15.41 Al-12.55Ni (Table 5.3). Although nickel is an austenite stabilizer, analysis of the EDS data highlights the enrichment of nickel, along with aluminum, in the B2 phase. This observation suggests that nickel demonstrates a stronger tendency to partition into the B2 phase when aluminum is present. In contrast, the B2 phase exhibits a lower manganese content compared to that of the austenite phase.

Table 5.3: Composition of features derived from the EDS spectrum.

Samples	Phases	Composition (mass %)				
		Fe	Mn	Al	Ni	Ni: Al
Base		63.62	18.95	10.51	5.88	1:3.88
PD3	Austenite	66.89	19.06	9.52	4.53	1:4.57
	Elongated B2	56.98	12.71	15.83	14.49	1:2.37
	Globular B2	58.53	14.09	15.13	12.25	1:2.68
PD3-A	Austenite	67.08	19.50	9.40	4.01	1:5.09
	Elongated B2	56.13	11.58	16.74	15.55	1:2.34
	Globular B2	58.17	13.87	15.41	12.55	1:2.67

5.2.4 EBSD analysis

The phase map derived from EDSD data of PD3 sample shows the volume percentages of austenite (red) and B2 phase (green) are 82.3% and 17.7%, respectively (Figure 5.5 (a)). On the other hand, in the PD3-A condition, the corresponding volume fractions of austenite and B2 phase are determined to be 72.3% and 27.3%, respectively (Figure 5.5 (b)). In case of PD3-AB_{30} the respective volume fractions of austenite and B2 are 78.4% and 21.6% (Figure 5.5 (c)). Notably, the volume fractions obtained from the EBSD are not similar to those calculated through XRD data analysis because of limited area in EBSD scan. The kernel average misorientation (KAM) maps derived from EBSD data shows that the average KAM values of PD3, PD3-A, and PD3-AB_{30} are 0.964° (Figure 5.5 (d)), 0.624° (Figure 5.5 (e)), and 0.67° (Figure 5.5 (f)) respectively. The image quality maps with superimposed grain boundaries of high-angle boundaries (HAGB) and low-angle grain boundaries (LAGB) displays that the LAGB percentage has decreased from 65.2% in the PD3 sample (Figure 5.5 (g)) to 58.9% in the PD3-A sample (Figure 5.5 (h)) to 54% in the

PD3-AB_{30} sample (Figure 5.5 (i)), while the HAGB fraction has increased from 31.7% in the PD3 sample (Figure 5.5 (g)) to 37% in the PD3-A sample (Figure 5.5 (h)) to 44% in PD3-AB_{30} sample (Figure 5.5 (i)). The misorientation angle versus the number fraction chart of the PD3 records a low average misorientation angle of 15.5° (Figure 5.6(a)). On annealing, the misorientation angle increases to 21.5° (Figure 5.6(b)). Due to low temperature ageing average misorientation angle increases further to 26° (Figure 5.6(c)).

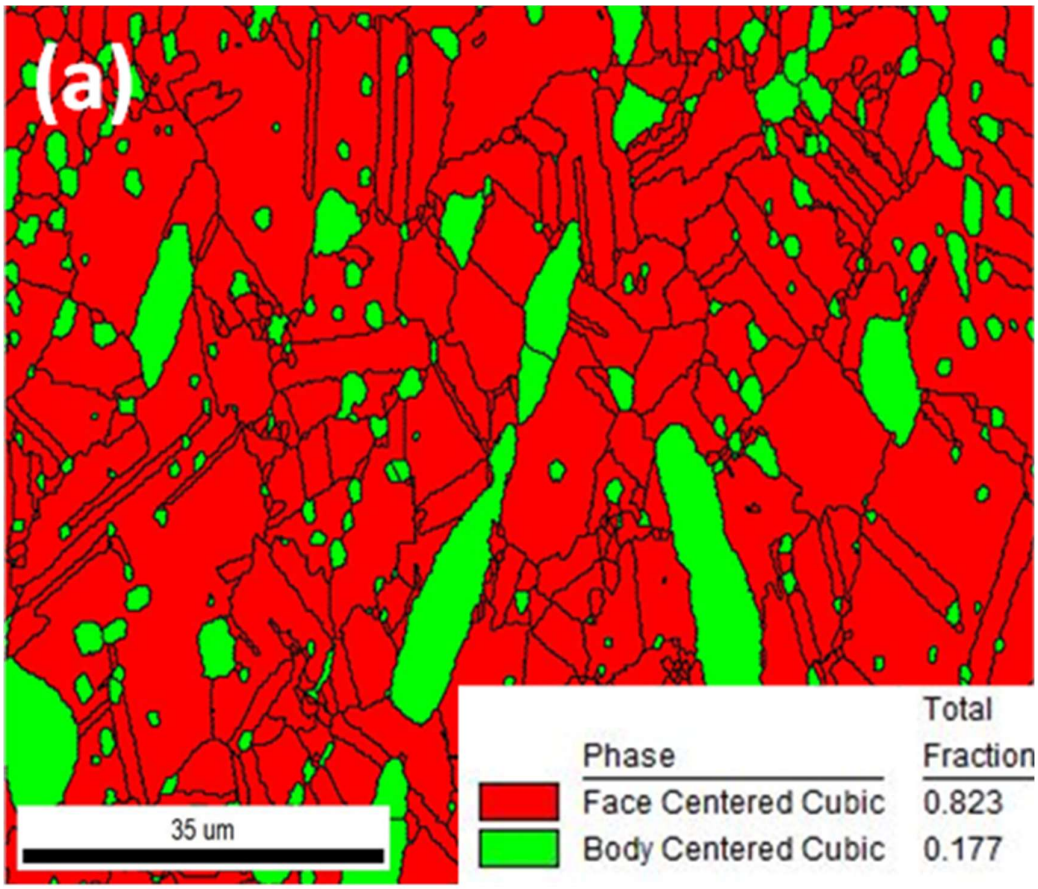

Figure 5.5: Phase maps (a, b, c), KAM maps (d, e, and f), and image quality maps with superimposed grain boundaries (g, h, i) for three samples: PD3, PD3-A, and PD3-AB_{30}. The color indicators used are red for austenite and green for the B2 phase. Blue represents the strain-free region whereas green and red represent strained regions.

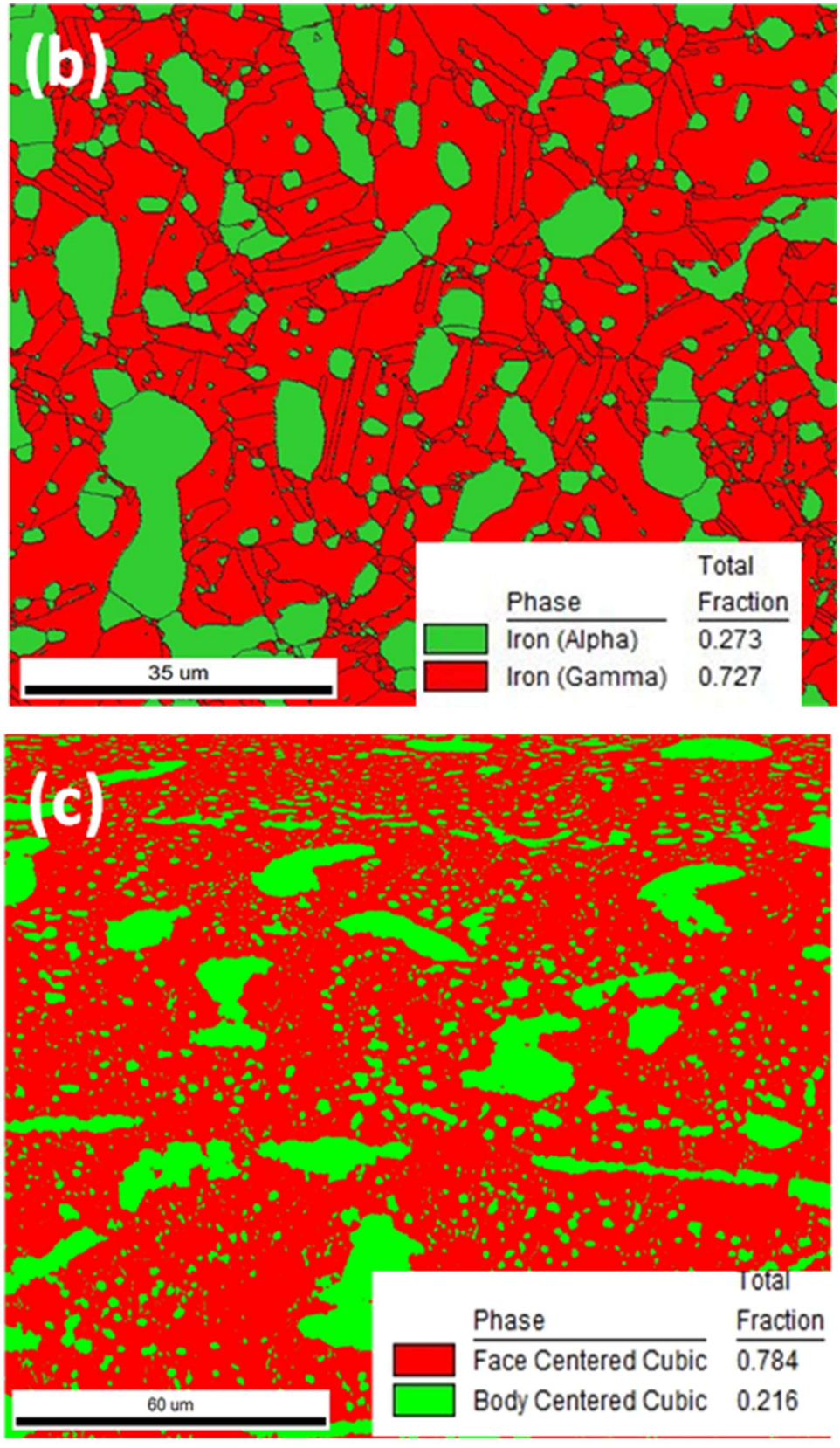

Figure 5.5: Continued.

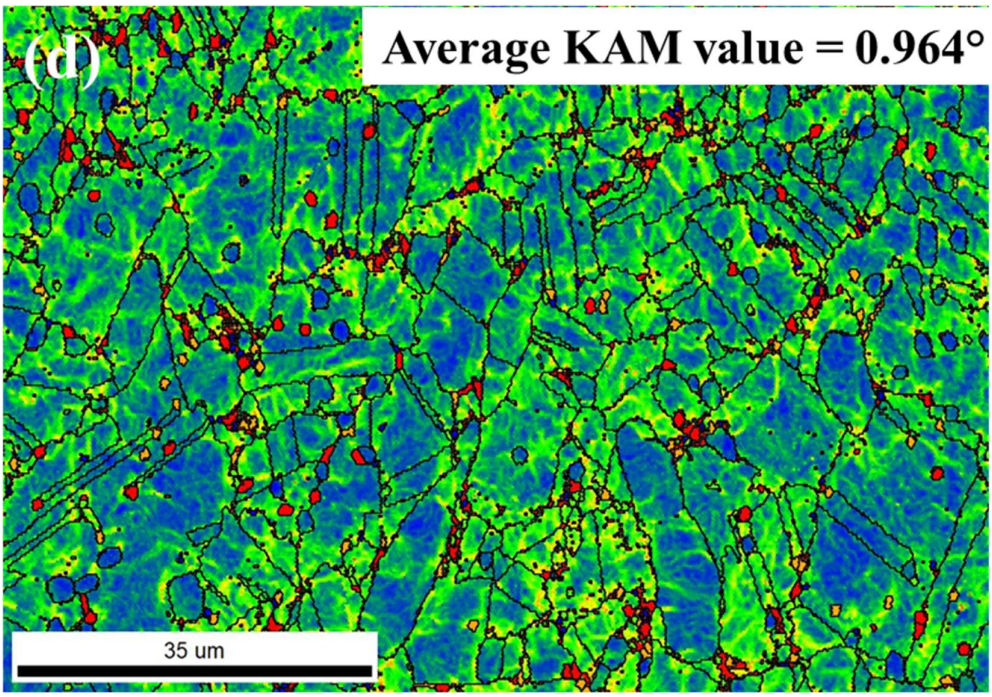

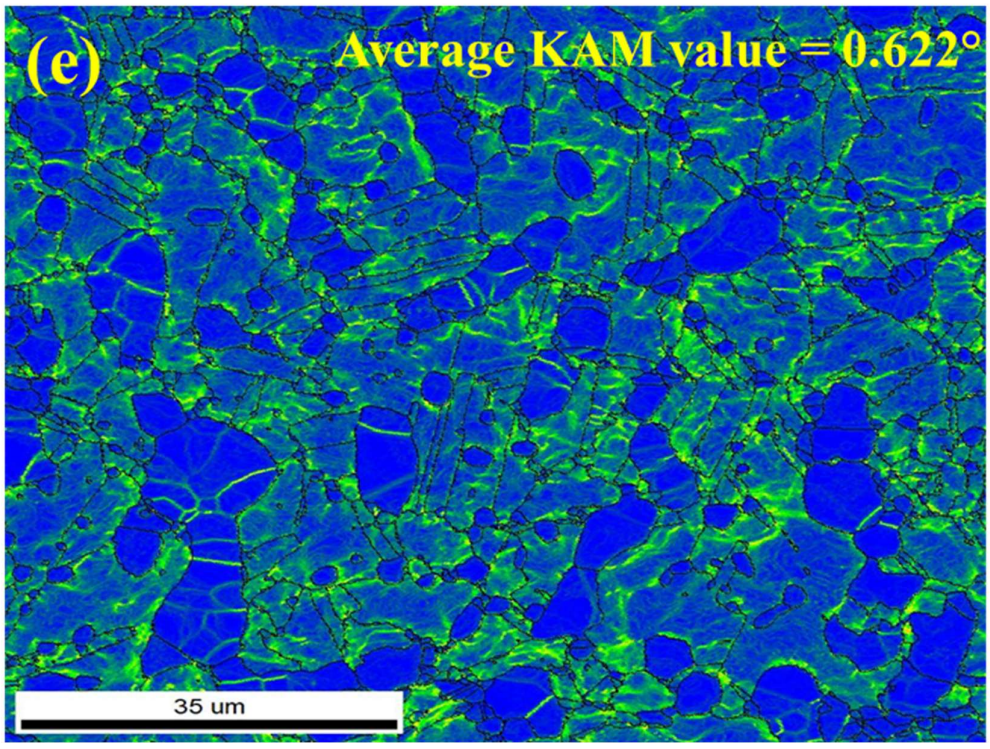

Figure 5.5: Continued.

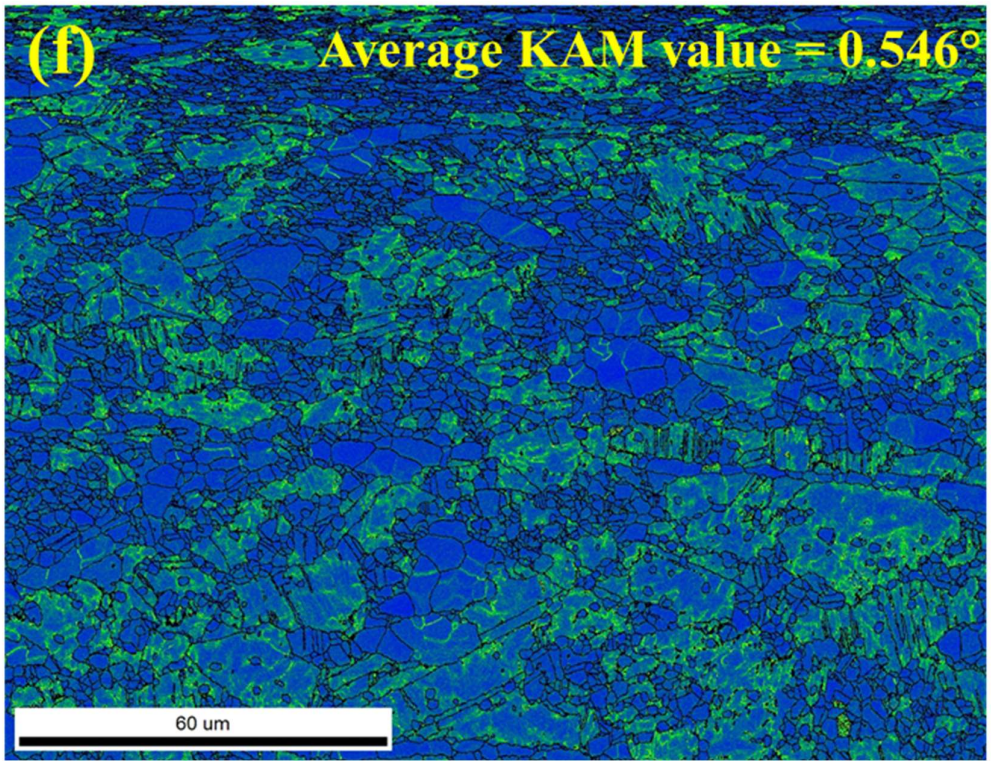

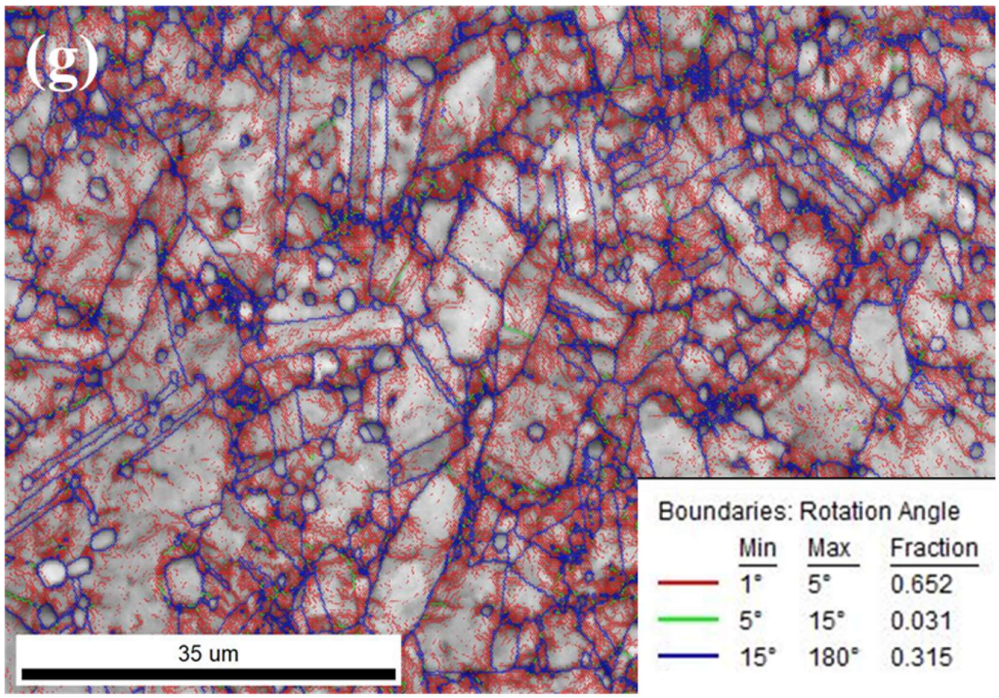

Figure 5.5. Continued.

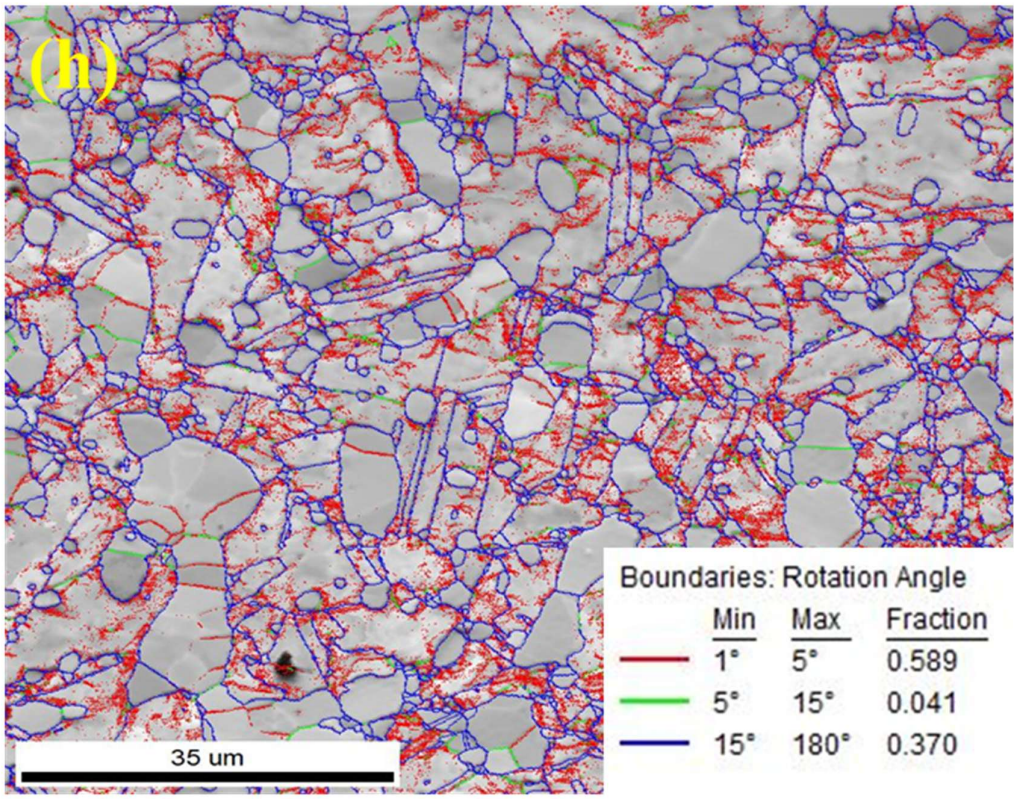

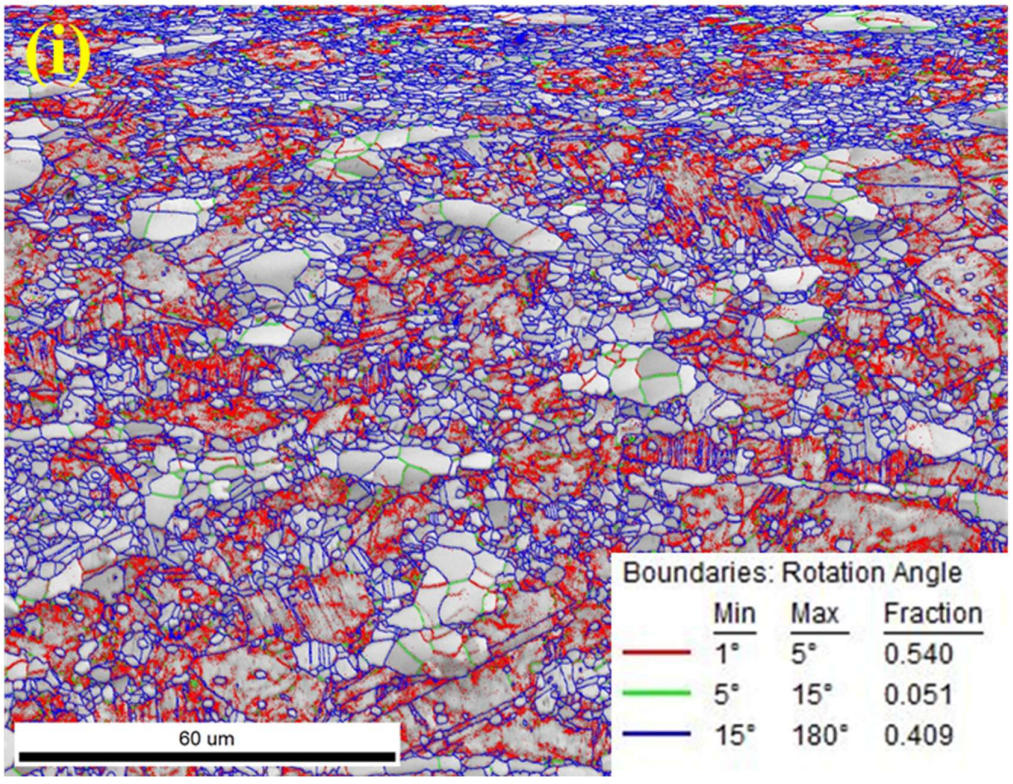

Figure 5.5. Continued.

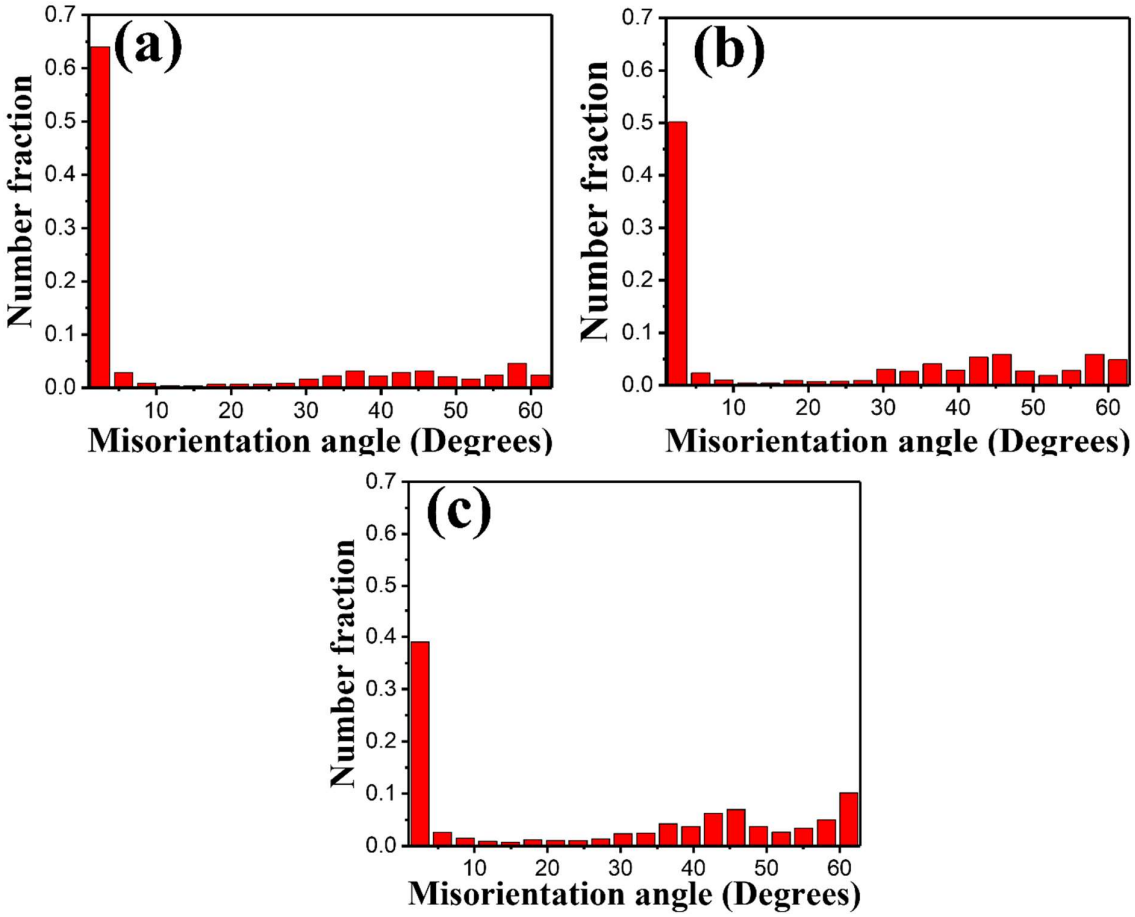

Figure 5.6: Misorientation angle vs. Number fraction chart of (a) PD3 (b) PD3-A and (c) PD3-AB30 samples.

5.2.5 TEM microstructure

The bright-field (BF) TEM micrograph of PD3-A (Figure 5.7(a)) presents mainly elongated grains with sub-grain structure and the selective area electron diffraction (SAED) pattern (Figure 5.7(b)) of the encircled region of the grain (in Figure 5.7(a)) confirmed to be of a face-centered- cubic phase which is austenite. A BF TEM image of another region reveals the presence of a platelet (Figure 5.7(c)). An SAED pattern (Figure 5.7 (d)) from the platelet confirms be ordered B2 phase. The B2 precipitates, with an approximate size of 250 nm, were present within the austenite matrix. B2 precipitates are also present in the

globular form. The BF TEM image of PD3-AB_{30} displays a pearlite-like structure (k-pearlite) between austenite grains (Figure 5.7(e)). The estimated volume fraction of k-pearlite is calculated at 5.9%, derived from the measurements of kappa carbide and ferrite widths, which are 35 ± 4.2 nm and 123 ± 19 nm respectively, as determined using ImageJ software.

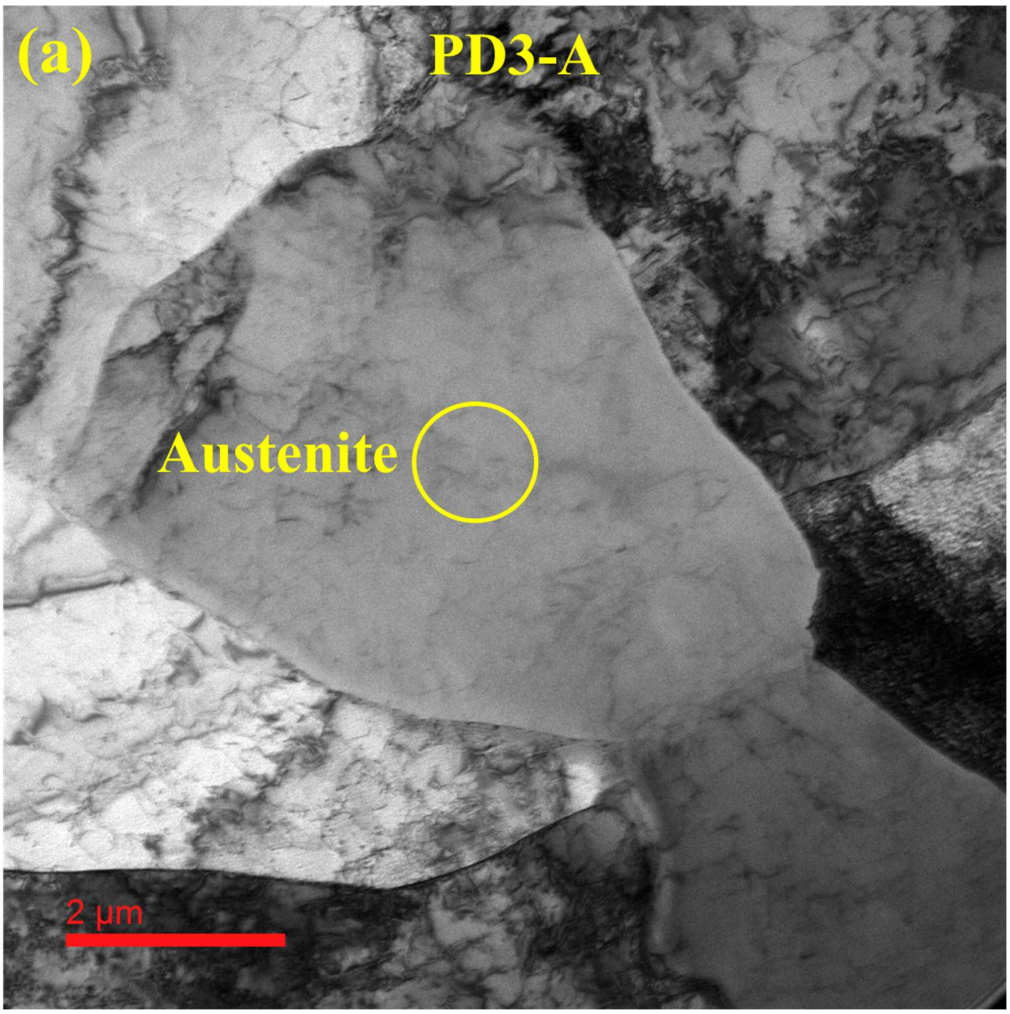

Figure 5.7: (a) BF TEM micrograph of PD3-A showing austenite by a circle, (b) SAED pattern of austenite of encircled area in (a) along [022$\bar{1}$] zone axis, (c) BF TEM micrograph of PD3-A displaying B2 precipitates in austenite matrix, (d) SAED pattern of B2 platelet along [001] zone axis, (e) BF TEM micrograph of PD3-AB_{30} revealing lamellar kappa carbide and ferrite at austenite grain boundaries.

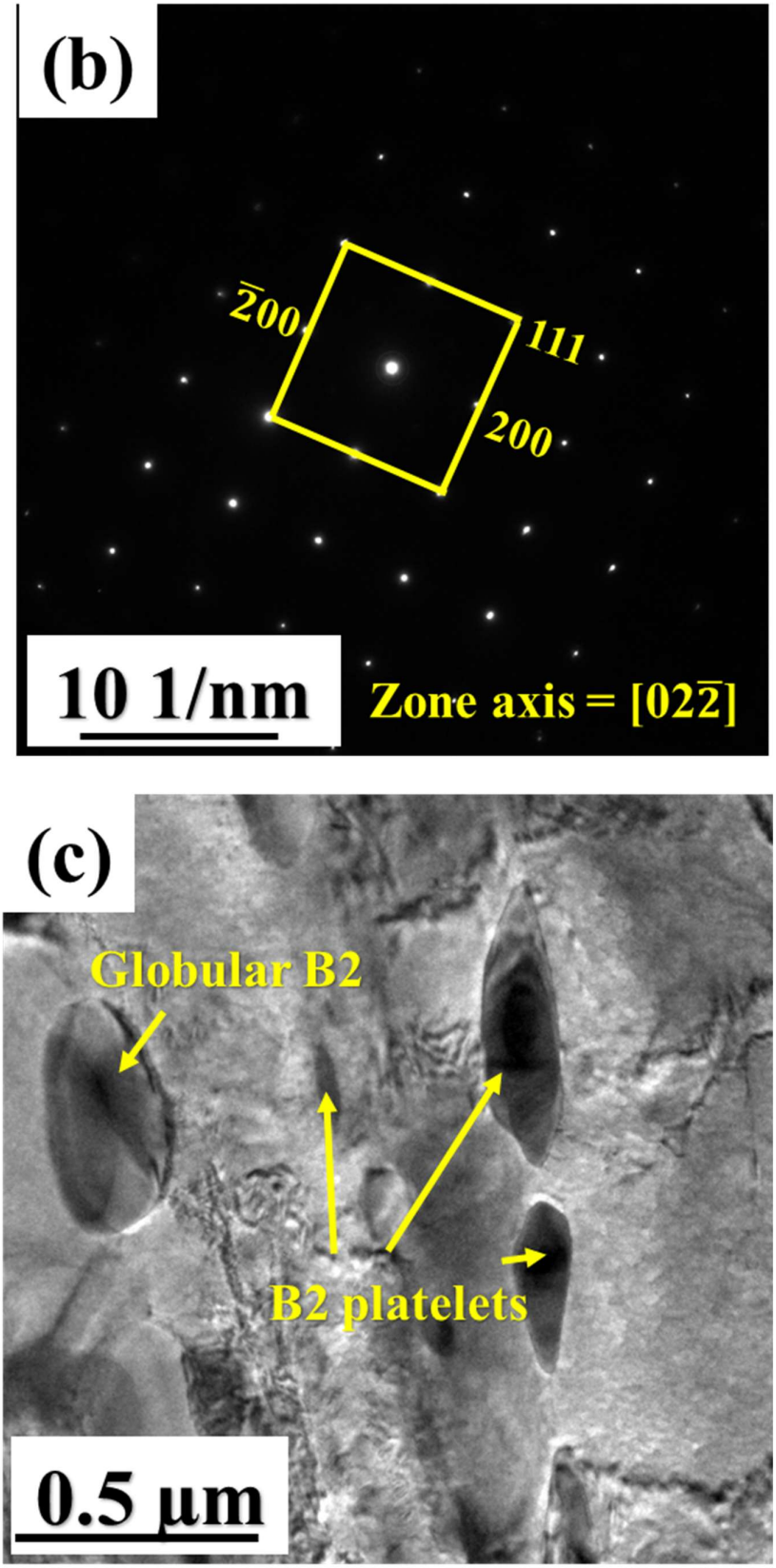

Figure 5.7. Continued.

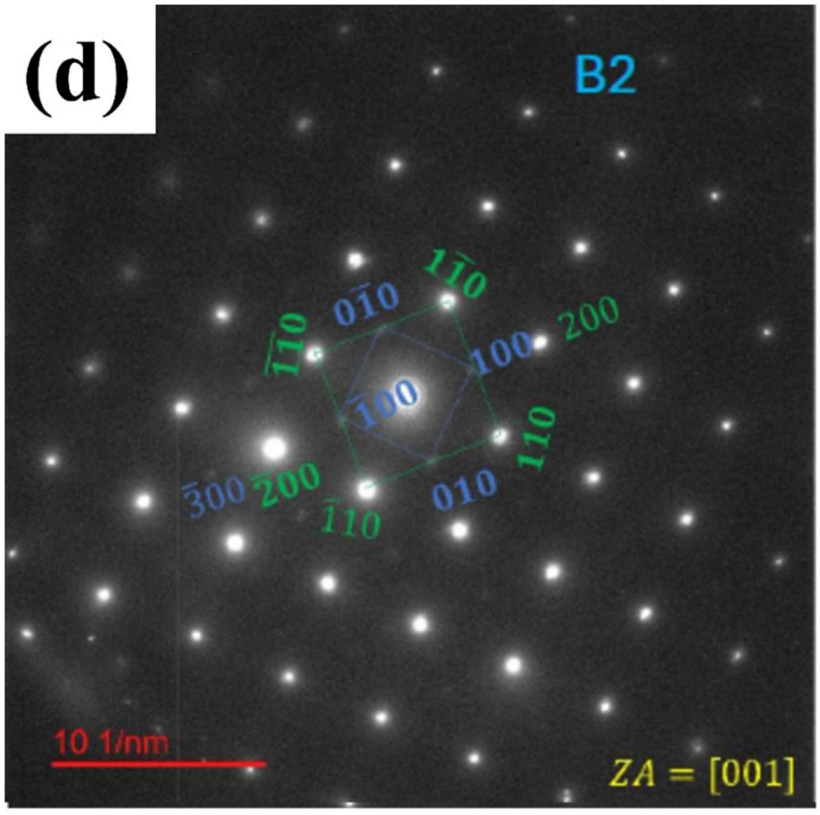

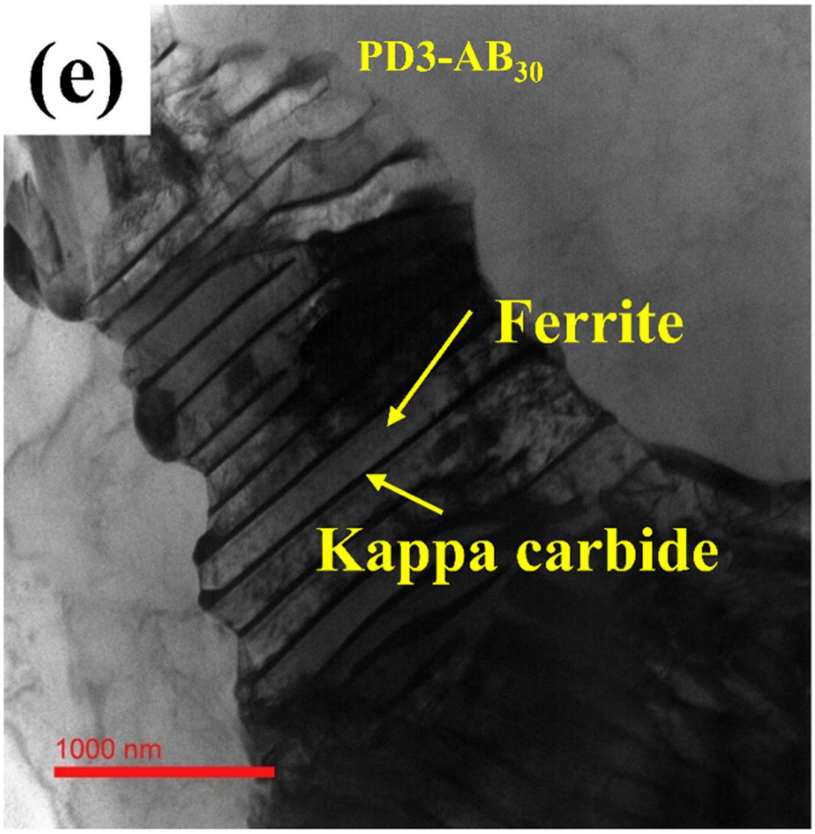

Figure 5.7: continued.

5.2.6 Tensile Properties

The engineering stress-strain curve of the PD3 sample (Figure 5.8(a)) shows that the material exhibits a yield strength (YS) of 1138 ± 20 MPa and an ultimate tensile strength (UTS) of 1296 ± 14 MPa, accompanied by a plastic elongation (PE) of 16.7 ± 0.5% (Table 5.4). In the PD3-A condition, the YS and UTS decreased to 1015 ± 13 MPa, and 1254 ± 40 MPa, with PE of 14.3 ± 2 % (Table 5.4). After aging at 550°C for 30 min, the YS and UTS increased to 1224 ± 11 MPa, and 1430 ± 18 MPa, respectively while the PE decreased to 9 ± 1.3 % (Table 5.4). The variation in the work hardening rate concerning the true plastic strain curves for PD3, PD3-A, and PD3-AB_{30} samples illustrates that there are three stages (stage I-stage III) of work hardening observed in PD3 and PD3-A but only stage I and stage II were found in PD3-AB_{30} (Figure 5.8(b)). The work hardening rates (θ_x) at the onset of stage I, II, and III are 4352 MPa, 2070 MPa, and 1863 MPa, respectively, for PD3 (Table 5.5). For PD3-A, the values are 7765 MPa, 2675 MPa, and 2186 MPa, respectively (Table 5.5). The work hardening rate for stage I and stage II in PD3-AB_{30}, are 8913 MPa and 2561 MPa, respectively (Table 5.5). The transition strains (ε_x) corresponding to the end of stages I, II, and III are 0.05, 0.1268, and 0.16361 for PD3 (Table 5.5). For PD3-A, the transition strain values are 0.0535, 0.1369, and 0.1602, respectively (Table 5.5). For PD3-AB_{30}, the transition strains for stage I to stage II is 0.061 and fracture occurs at a true strain of 0.1008 (Table 5.5). A continuous decrease in the work hardening rate with increasing strain is observed in all the samples. In PD3 and PD3-A, the work hardening rate decreases sharply in stage I followed by a constant work hardening in stage II and later with dynamic recovery in stage III. Both PD3-A and PD3-AB_{30} display substantially higher work hardening rates in comparison to that of respective stages in PD3.

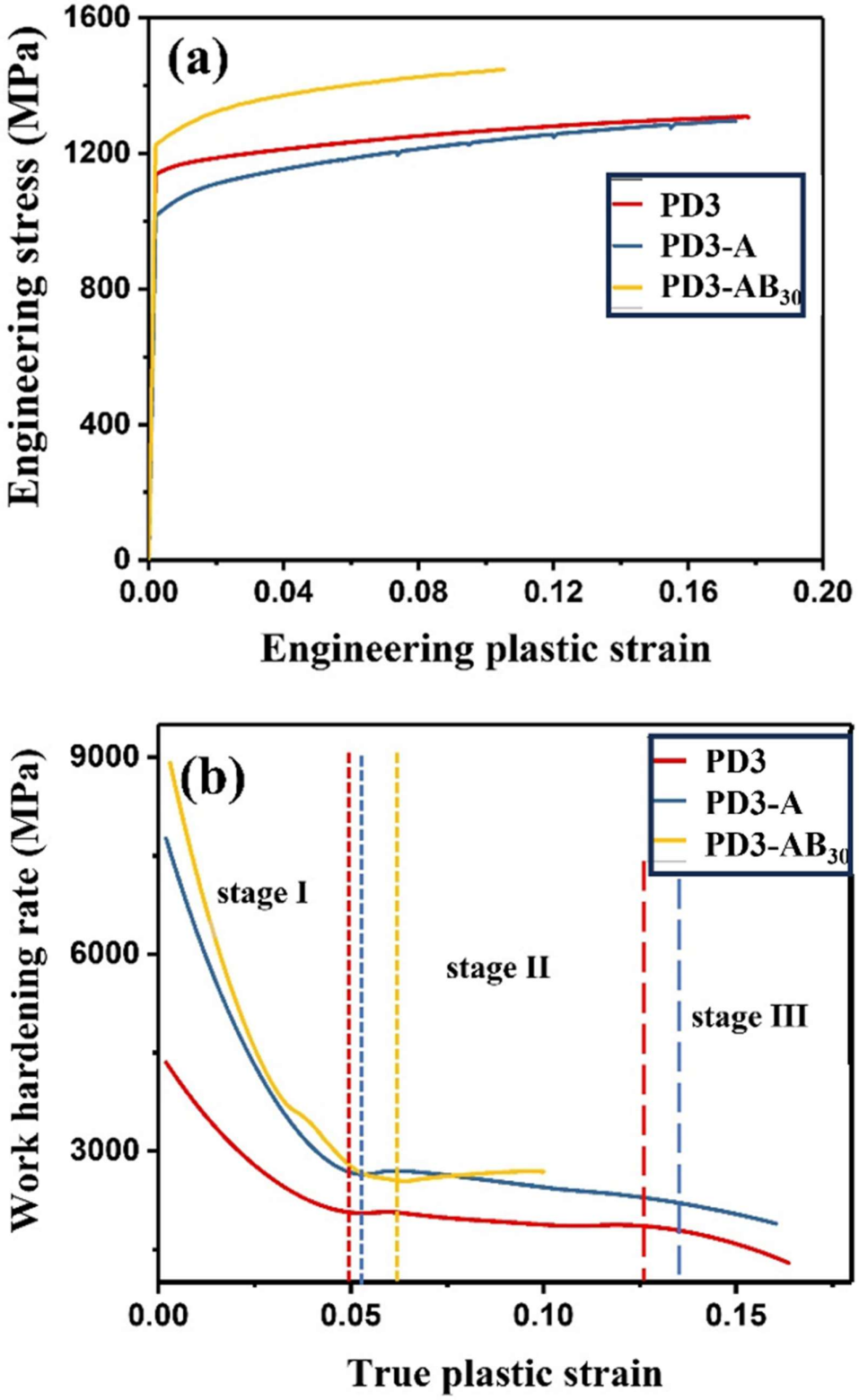

Figure 5.8: (a) Engineering stress-strain diagram, (b) work hardening rate vs true plastic strain of PD3, PD3-A, and PD3-AB_{30} samples.

Table 5.4: Tensile properties of PD3, PD3-A and PD3-AB_{30} low-density steels.

Sample	YS (MPa)	UTS (MPa)	Plastic elongation	Specific YS (MPa.cc /g)	Specific UTS (MPa.cc /g)
PD3	1138 ± 20	1296 ± 14	16.7 ± 0.5	170.6	194.3
PD3-A	1015 ± 13	1254 ± 40	14.3 ± 2	152.2	188
PD3-AB_{30}	1224 ± 11	1430 ± 18	9 ± 1.3	209.6	223.8

Table 5.5: Work hardening rate at the start and the true strain at the end of stages I, II, and III for PD3, PD3-A, and PD3-AB_{30}.

Material	θ_1 (MPa)	θ_2 (MPa)	θ_3 (MPa)	ε_1	ε_2	ε_3
PD3	4352	2070	1863	0.05	0.127	0.164
PD3-A	7765	2675	2186	0.054	0.137	0.160
PD3-AB_{30}	8913	2561	--	0.061	0.101	--

The superimposed curves derived from the Hollomon, Ludwik, swift, Ludwigson and voce flow equation models with experimental true stress versus logarithmic true plastic strain curves of PD3, PD3-A, and PD3-AB_{30}, respectively are displayed in Figures 5.9 (a), (b), and (c). Among the various fitted models, the Ludwigson model was found to be the best fit for the experimental curves, as evidenced by the highest R^2 (coefficient of determination) and the lowest χ^2 (sum of squares of deviation of calculated stress values from experimental stress values) values for each type of material (Table 5.6). At a low strain regime, the strength coefficients (exp(K1)) for PD3, PD3-A, and PD3-AB_{30} are 1118 MPa, 916 MPa, and 1043 MPa, respectively. The corresponding work-hardening exponents(n1) are -1.09, -1.60, and -1.90, respectively. At high strain regimes, both PD3

and PD3-A show similar strength coefficients (K) 566 MPa and 575 MPa respectively, whereas it decreased for PD3-AB_{30} of 431 MPa. The work hardening coefficients (n) are decreased from PD3 to PD3-A to PD3-AB_{30} from 0.59 to 0.30 to 0.03.

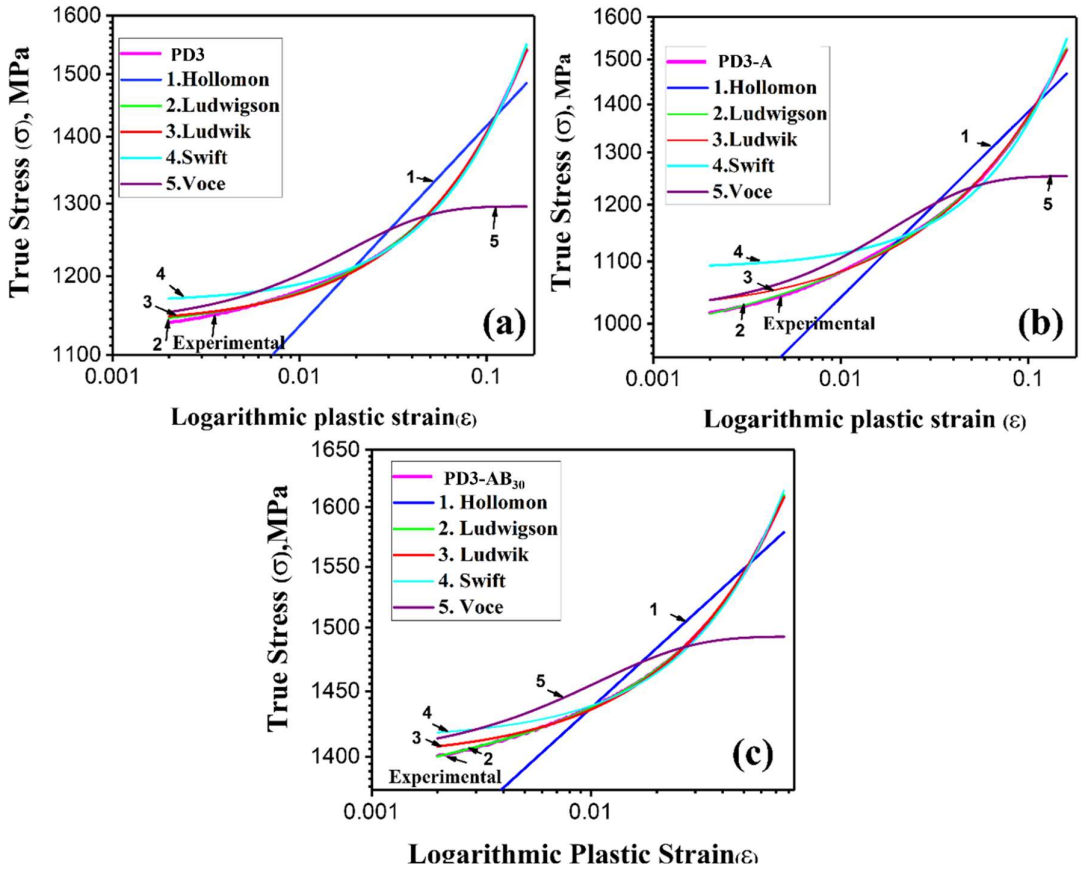

Figure 5.9: Experimental true stress- logarithmic plastic strain curves of (a) PD3 (b) PD3-A and (c) PD3-AB_{30} fitted with various flow equations.

Table 5.6: Strength coefficients, work-hardening exponents, and fitting parameters with Ludwigson flow equation for PD3, PD3-A, and PD3-AB_{30} samples.

Sample	exp(K1) (MPa)	n1	K (MPa)	n	R^2	χ^2
PD3	1118	-1.09	566	0.59	0.9999	1.1789
PD3-A	916	-1.60	575	0.30	0.9998	2.2564
PD3-AB_{30}	1043	-1.93	431	0.03	0.9999	0.13878

5.2.7 Fractography

The SEM fractograph of PD3 displays dimples of area percentage of 71% and its size of 2.3 ± 0.6 µm and 29% facets (Figure 5.10 (a)). The fractography of PD3-A shows dimples of area percentage of 45% and its size of 1.7±0.5 µm and 55% facets (Figure 5.10 (b)). The fracture surface of PD3-AB_{30} presents dimples of area percentage of 32 % and its size 1± 0.5 µm and 68% facets (Figure 5.10 (c)). The size of dimples and the area percentage of dimples & facets are presented in Table 5.7.

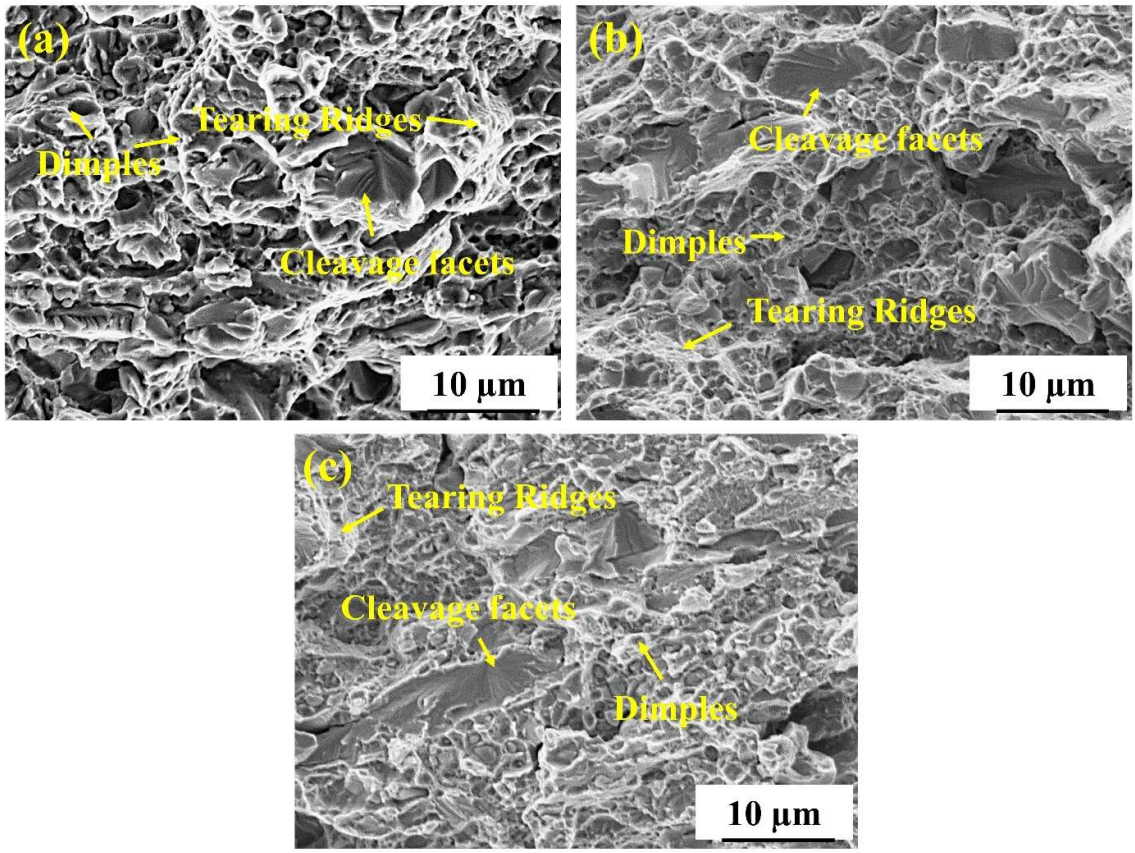

Figure 5.10: SEM fractographs of the samples (a) PD3 (b) PD3-A and (c) PD3-AB30 depicting cleavage facets and dimples.

Table 5.7: Size of dimples and facets in fractographs.

Material	Dimple size, (μm)	Dimple area percentage	Facets area fraction
PD3	2.3 ± 0.6	71	29
PD3-A	1.7 ± 0.52	45	55
PD3-AB_{30}	1.0 ± 0.54	32	68

5.3 Discussion

Till now about a maximum of 5 mass% Ni is added in high carbon low-density austenite-based duplex steel. While materials are hot rolled followed by cold rolled short annealing at low temperature the microstructure contains an optimum quantity of B2 and distribution which leads to high tensile strength and reasonable ductility but cold rolling cost is added [54], [70], [80], [82]. If cold rolling is avoided, annealing at 500-900°C, yield strength and tensile strengths are low with low ductility but with increasing temperature of annealing to 1050°C strengths as well as ductility are higher [72], [73]. While austenite-based low density steels of high Mn, C, and Ni, were hot rolled followed by cold rolling and short annealing, the materials reported higher strength and ductility due to refined precipitates of B2 and κ carbide [75]. It is worth studying duplex low-density steel with enhanced Ni content and avoiding cold rolling but continuing with annealing to get high strength and ductility. While materials are hot rolled, and air-cooled followed by short annealing and short aging, the LDS reports a good combination of high strength and high ductility. Therefore, there is the possibility of getting high strength and high ductility without undergoing any cold rolling [76]. The materials contain very high B2 (>30%), for lower Mn, hot rolling followed by cold rolling results in low tensile strength [78]. While austenite-based low-density steel of high Mn, C with 5% Ni, were hot forged, and annealed

at high temperature for a long time followed by hot rolling at 900-1050°C and air cooling, the material contains a low amount of B2 and κ carbides with high dislocation density. The material displays a good combination of high strength and ductility [79]. Therefore, it is worth getting a small amount of B2 with high dislocation density by hot rolling at low temperatures and water quenching to avoid carbide precipitation in grain boundary which may result good combination of high strength and ductility.

The main focus of this study was to develop a material with a 15% reduction in density compared to conventional steels, which is a desirable property for its potential applications in the automotive industry. To achieve this objective, the material has been designed by incorporating higher amounts of aluminum of 10.5 mass %, which results in a lower density of 6.67 g/cc with a slight contribution from the remaining alloying elements. A multi-step hot rolling process with a reduction in thickness of 75% has been employed, followed by water quenching to breakdown the as-cast structure of the material. Specifically, the water quenching step plays a vital role in preventing the formation of kappa carbides along the grain boundaries. Previous studies have shown that both intergranular and intragranular kappa carbides (κ-carbides), which form during the slow cooling process along the austenite grain boundaries and within the austenite matrix respectively, have a detrimental effect on the ductility and toughness of the material [20], [45] . The size of the kappa carbides (κ-carbides), which form during the slow cooling process along the austenite grain boundaries and within the austenite matrix, is estimated to be 3-6 times larger than the carbides formed after the process of solutionizing, quenching, and aging, as described in the reference [20], [45]. No cold rolling process is employed after hot rolling to decrease the cost and labor involved in the process.

5.3.1 Microstructure

As-cast material has austenite of disordered FCC and δ ferrite of disordered BCC phases as confirmed by the X-ray diffraction pattern (Figure 5.1(b)). The XRD pattern of homogenized and hot rolled (PD3) low-density steel displays the presence of disordered austenite and ordered B2 phase containing weak superlattice reflection at 100 planes (Figure 5.4). It indicates that during the homogenization treatment, disordered δ ferrite got transformed into B2 through ordering. The equilibrium phase diagram obtained from ThermoCalc calculations also shows the transformation of disordered δ ferrite into ordered B2 phase at temperatures below 1242 °C. As the homogenization and hot rolling are conducted in the temperature range of 1200°C-950°C, there is complete disappearance of δ ferrite and only ordered B2 phase field along with austenite are present. Therefore, the optical micrograph of as-cast low-density steel (Figure 5.2(a)) shows the presence of austenite and δ ferrite whereas PD3 (Figure 5.2(b)) has austenite and only ordered B2 phase. There is no disordered δ ferrite in PD3. In the optical micrograph of PD3, elongated (banded) and globular morphologies of B2 can be observed. The B2 grains become elongated as a result of the deformation caused by the hot rolling process. The hot rolling temperatures are not high enough to fully recrystallize the B2 phase, which formed due to ordering in δ ferrite. This is because the presence of a significant amount of aluminum increases the stability domain of the δ ferrite phase, thereby increasing the recrystallization temperature of δ ferrite [17], [20]. During hot rolling, some of the austenite grains undergo recrystallization, while others become deformed (elongated γ, as indicated in Figure 5.2(b)). This phenomenon is attributed to the inhomogeneous nature of deformation that occurs at the microscopic level, leading to different recrystallization kinetics at that particular level. Kim showed that when localized recrystallization proceeds quickly during thermomechanical deformation, the fine B2 particles precipitate at recrystallized austenite

grain boundaries [54]. The reason for the formation of globular B2 at grain boundaries, as shown in Figure 5.2(b), might be due to the localized rapid recrystallization of austenite grains. Some localized intense deformation zones are also present in non-recrystallized austenite grains, indicated as deformation bands.

The microstructure observed after annealing at 930°C for 30 min (PD3-A) depicted fine B2 precipitates, as well as coarser plate-like precipitates. The coarsening of B2 platelets along the deformation bands as shown in Figure 5.3 (b). As seen from the micrograph, only along the deformation band, the B2 platelets are coarsened, whereas within the matrix, there is the presence of very fine B2 platelets. The coarsening along the deformation bands is due to the increased diffusion of elements compared to that formed within the matrix, which aligns with the findings reported by Song et al. [132]. The size and morphology of these B2 precipitates are consistent with the findings reported in previous studies [54], [72]. While it is known that nanoscale B2 precipitation contributes to increased material strength, the occurrence of coarse B2 precipitates has been observed to significantly reduce ductility [133]. The observed microstructural evolution is consistent with the findings reported by Kim et al. [2015], who identified three types of B2 phase morphologies: stringer bands, fine B2 particles at phase boundaries, and finer globular particles within austenite grains and along shear bands. According to Balluffi [134], the diffusion of Ni and Al along dislocations requires a lowering of activation energy compared to bulk diffusion. This difference in activation energy results in the accelerated diffusion of Ni and Al, leading to the coarsening of precipitates along deformation bands.

According to the simulated phase diagram generated by ThermoCalc, the predicted equilibrium volume fractions of austenite and B2 phases at 950°C are 70.5% and 29.5%, respectively. At 930°C, these fractions are 70.8% and 29.2%, respectively. However, the XRD patterns shown in Figure 4 indicate that at 950°C, the volume fractions are 87% and

13% for PD3. At 930°C, the volume fractions are 82% and 18%, for PD3-A, respectively. The increase in the volume fraction of B2 at 930°C can be attributed to the precipitation of platelet-type B2. With longer soaking times, there may be further increases in the B2 phase, aligning with the predicted volume fractions from the simulated phase diagrams. The differences of approximately 17% in PD3 and 12% in PD3-A could be due to the incomplete establishment of accurate thermodynamic databases for the Fe-Mn-Al-C-Ni system [20]. The micro strain values, determined using Scherrer's equation with XRD data, indicate that the austenite phase displays lower strain compared to B2. This implies that the austenite phase undergoes a greater degree of recrystallization during hot rolling and subsequent heat treatments, resulting in a decrease in strain distribution. Furthermore, the dislocation density values also support this finding, as the B2 phase exhibits a higher dislocation density compared to the austenite phase. X-ray diffraction (XRD) analysis confirmed the presence of kappa carbide precipitates in the aged condition (PD3-AB_{30}).

The EDS data presented in Table 5.3 reveal that compared to the austenite phase, there was enrichment of nickel and aluminum in the B2 phase under all processing conditions. Although nickel is typically used as an alloying element to stabilize the austenite phase, the EDS analysis indicates that nickel is partitioned into the B2 phase in this particular alloy. The carbon contents in austenite are estimated assuming that the maximum solubility of carbon in B2 is 0.17 % C. The resultant carbon contents in austenite of PD3, PD3-A, and PD3-AB_{30} are 1.17%, 1.32% and 1.25% respectively. The phase maps as shown in Figure 5.5 (b) support this finding by demonstrating an increased volume fraction of the B2 phase after annealing at 930°C for 30 min. The B2 phase is characterized by the precipitation of ordered phases with higher nickel and aluminum contents. This conclusion is further supported by the diagram calculated using Thermo-Calc software, as depicted in

Figure 5.1, which illustrates a decrease in the volume fraction of austenite and an increase in the volume fraction of the B2 phase with increasing temperature.

Kernel Average Misorientation (KAM) values, representing the average misorientation between a point and its closest neighbors within the same grain, serve as a measure of local misorientation [135]. Larger KAM values observed on the KAM maps suggest the presence of higher cumulative strain [136], indicating a higher density of geometrically necessary dislocations [137]. The KAM maps as depicted in Figure 5.5(d) offer qualitative evidence of higher strain accumulation in the hot-rolled steel compared to that of the annealed steel. After undergoing a heat treatment at 930°C for 30 min, the strain distribution was reduced due to the annihilation of dislocations. Figure 5.5 (g, h, i) provides insight into the grain boundaries present in the hot-rolled and water-quenched material, showing a significant volume fraction of low-angle grain boundaries and a smaller volume fraction of high-angle grain boundaries. Materials with high stacking fault energies typically exhibit a dominant process of dynamic recovery. During hot rolling, the continuous dynamic recrystallization process takes place, which involves dynamic recovery, rearrangement, and annihilation of dislocations at elevated temperatures. This process leads to the formation of a significant number of sub-grain boundaries. The heat treatment at 930°C was found to increase the fraction of high-angle grain boundaries by more than 10% through the coalescence of sub-grain boundaries. Annealing at 930°C provided a suitable temperature for the formation of large-angle grain boundaries. Subsequently, during ageing conditions, a higher fraction of high-angle grain boundaries was observed.

The ordered B2 platelet formed during annealing is confirmed by the superlattice reflections shown in Figure 5.7 (d). After aging the material at 550°C (PD3-AB_{30}), lamellar type kappa carbide and ferrite precipitation has been observed near the grain boundary of austenite (Figure 5.8 (e)). In lightweight steels, Fe-(18-30)Mn-(6.5-11)Al-(0.8-1.3)C,

coherent kappa-carbides of approximately 2 to 10 nm in size form uniformly inside the austenitic grain (intragranular) through spinodal decomposition [56], [138]. This process takes place during aging at temperatures between 450°C and 650°, typically lasting from 1 hour to several hours [20]. When aging at high temperatures of 650°C - 850°C, kappa carbide precipitation takes place intergranularly with various morphologies, such as rod type, globular type, and lamellar type [20], [33]. When aging is performed at low temperatures but for a long duration significant precipitation also occurs at the grain boundary. In the case of nickel-added low-density steels, intra-granular precipitation of kappa carbide takes place at the temperature range of 550°C-800°C [75]. The precipitation of kappa carbides also occurs at grain boundary at a temperature as low as 530°C [83], [139]. Piston observed that in Fe-18Mn-10Al-0.9C-5Ni, after aging at 530°C, the formation of lamellar kappa carbide precipitates occurred at the grain boundary, with an interlamellar spacing of 600 nm [83]. Zargaran noticed that in Fe-21Mn-10Al-1C-5Ni, the formation of cuboid-type intragranular kappa carbide of size 50 nm and rod-type intergranular kappa carbide of 100 nm in size takes place after aging at 550°C [76]. Zhang et al., found both cuboid/spherical intragranular and rod-like intergranular kappa carbides of the typical size range of 55 nm-280 nm and 150 nm-730 nm, respectively in Fe-16.36Mn-8.94Al-0.84C-3.02Ni, aged at 600°C [139].

Previous studies in Fe-13.5Mn-6.3Al-0.78C alloy have shown that the lamellar mixture of kappa carbide and α ferrite via cellular transformations and eutectoidal decomposition [33]. While steel is isothermally held above eutectoid temperature (typically 800°C) austenite decomposes to proeutectoid α and kappa carbide in cells or granular or globular form and diluted retained austenite by cellular transformation near to austenite grain boundary [33]. Precipitates grow by grain boundary migration into the austenite matrix as small nodules which take lamellar morphology at a later stage. The epitaxial type/rod type structure of k-

carbide takes place along the plane of the boundary between k-carbide and ferrite for lowering the strain energy [140]. When the retained austenite or supersaturated austenite is isothermally held at a temperature below eutectoid temperature 650-625°C, the austenite near grain boundary decomposes into lamellar α and kappa carbide as k-pearlite by eutectoidal transformation.

Rana et al., has also shown in Fe-6.57Al-3.34Mn-0.18C that the growth of kappa carbide and α ferrite is an epitaxial type [22], [140]. Zhao et al., has shown that the austenite phase is eutectoidally decomposed into ferrite and kappa carbide completely when aged the Fe–10Mn–10Al–0.7C alloy at 700°C for 1 h [140]. In the present investigation, while PD3-AB_{30} is isothermally held at 550°C well below the eutectoid temperature of 613°C, the supersaturated austenite decomposes to k-pearlite eutectoidally.

Based on the phase diagram, it can be inferred that when the alloy undergoes aging at a temperature of 550 °C, the stable phases observed are austenite, ordered B2, disordered A2, and kappa carbide. At this specific temperature, the austenite phase decomposes into disordered A2 ferrite and kappa carbide. The disordering of B2 does not occur at this particular temperature due to the low diffusion coefficient of nickel, which ultimately promotes the stability of the ordered B2 phase until room temperature, as indicated by the phase diagram. From the phase diagram, it can also be observed that the formation of ferrite and kappa carbide, collectively referred to as simple k-pearlite, takes place at temperatures below 590°C. It is evident from the TEM image (Figure 5.7 (e)) that the lamellar ferrite and κ-carbide nucleate and grow concurrently at the grain boundary, progressing toward the austenite matrix as κ-pearlite colonies. It can be confirmed that the growth of the ferrite and kappa carbide phases is cooperative [33]. Initially, the manganese and carbon contents present in the ferrite phase are rejected into the surrounding austenite matrix, while the aluminum atoms in the austenite phase are consumed by the ferrite phase, leading to its

growth. Consequently, regions adjacent to the ferrite grains provide suitable conditions for the growth of κ-carbide grains with a high concentration of manganese and carbon. As the κ-carbide phase develops, the neighboring austenite regions experience a depletion of aluminum, manganese, and carbon atoms. Therefore, regions with low concentrations of manganese and carbon solutes are preferred sites for the growth of ferrite.

5.3.2 Mechanical properties

At an early stage of aging up to 30 min the increase in hardness is attributed to the precipitation of k-pearlite, but beyond 30 min, the hardness starts to decrease due to the coarsening of the precipitates.

5.3.2.1 Strengthening mechanisms

Contribution of various strengthening mechanisms to the yield strength of PD3:

The yield strength (σ_γ) of austenite in low-density steel is a function of friction stress (σ_p) (Peierls stress) and strengthenings by solid solution (σ_{ss}), dislocations (σ_{dis}), and grain boundary (σ_{gb}) which is given by Equation 5.1 [50].

$$\sigma_\gamma = \sigma_p + \sigma_{ss} + \sigma_{dis} + \sigma_{gb} \quad [5.1]$$

The friction stress (σ_p) is the sum of Peierls stress components which is calculated from the shear stress (τ_0) required to move a dislocation in a single crystal and is given by [116], [117].

$$\sigma_P = 3 * 2*10^{-4} G \quad [5.2]$$

Where G is the shear modulus.

Taking G as 70 GPa for austenite for a similar composition [78], the σ_P is estimated to be 42 MPa.

The solid solution strengthening ($\sigma_{\gamma ss}$) from austenite is calculated using Equation 5.3 [70].

$$\sigma_{\gamma ss} = 279 * wt.\%C - 1.5 * wt.\%Mn + 20.5 * wt.\% Al + 2.9 * wt.\% Ni \quad [5.3]$$

$\sigma_{\gamma ss}$ is calculated to be 506 MPa.

The dislocation density contribution to the strength (σ_{dis}) is formulated by Taylor as shown in Equation 5.4 [118].

$$\sigma_{dis} = M\alpha Gb\sqrt{\rho} \quad [5.4]$$

Where M is the average Taylor factor, α is the Taylor constant, and b is Burger's vector. Taylor factor (M) is analyzed using EBSD i.e., as 3.05. Taylor constant α is 0.24 for austenite [119]. Burger's vector is calculated by using XRD data to be 2.6 Å. The dislocation density contribution to austenite is calculated to be 390 MPa.

The grain boundary contribution to yield strength (σ_{GB}) is determined using Equation 5.5.

$$\sigma_{GB} = K_B . d^{-1/2} \quad [5.5]$$

where K_B is the grain boundary locking parameter which is taken as 330 MPa.$\mu m^{1/2}$ for similar alloy [78] and d is grain size of austenite in μm. The estimated σ_{GB} is 122 MPa.

The total strength contribution from the austenite phase (σ_{γ}) (by considering the presence of 100% austenite) is calculated to be 1060 MPa.

Taking G as 88 GPa for B2 [141], the estimated σ_P for B2 is 53 MPa by using Equation 5.2.

The contributions of solid-solution strengthening (σ_{B2ss}) of B2 is calculated using Equation 5.6 [142].

$$\sigma_{B2ss} = 1103 * wt.\%C + 16.9 * wt.\%Mn + 9 * wt.\%Al + 19.2 * wt.\%Ni \quad [5.6]$$

The solid solution strengthening contribution from B2 (σ_{B2ss}) is estimated to be 822.9 MPa.

The calculated σ_{dis} of B2 is 550 MPa by using Equation 5.4 considering the Taylor factor as 2.754 and burgers vector as 2.5 Å.

The estimated σ_{GB} is 99 MPa by considering K_B as 745 MPa μm$^{1/2}$ for B2 [143].

The total calculated strength contribution to yield strength from B2 (σ_{B2}) is 1525 MPa.

Therefore, the total yield strength σ_{PD} for PD3 is determined by a weighted average of austenite and B2 phases which is given as Equation 5.7.

$$\sigma_{PD3} = \sigma_{\gamma} * f_{\gamma} + \sigma_{B2} * f_{B2} \quad [5.7]$$

Therefore, σ_{PD1} is calculated to be 1137 MPa, which is near the experimental yield strength of 1138 MPa. The major contribution to yield strength comes from solid solution strengthening followed by dislocation strengthening and second phase strengthening from B2. The contribution of various strengthening mechanisms to the overall yield strength of PD3 is given in Table 5.8.

Contribution of various strengthening mechanisms to the yield strength of PD3-A:

The yield strength of austenite $\sigma_{\gamma PD3}$ in PD3-A is calculated using Equations 5.1-5.5 considering composition, grain size, and dislocation density and the calculated value is 941MPa.

Similarly, the yield strength of coarse-sized banded and globular B2 is estimated using Equations 5.1-5.2, 5.4-5.6 and the calculated value is found to be 1389 MPa.

An additional 5 % B2 platelet contributes to the strengthening of the alloy by the Orwan bowing mechanism. The contribution is calculated by using Equation 5.9 [144].

$$\sigma_{ppt} = 0.12\, MG \frac{b}{\sqrt{DT}} \left(\sqrt{f} + 0.7 \sqrt{\frac{D}{T}} f + 0.12 \frac{D}{T} f^{1.5} \right) \ln \left(\frac{0.079D}{b} \right) \quad [5.9]$$

Where D and T are the average width and thickness of the B2 platelet and f is the volume fraction.

The σ_{ppt} is estimated as 23 MPa and for the yield strength of the alloy Equation 5.7 is modified to Equation 5.10.

$$\sigma_{PD3-A} = \sigma_{\gamma} * f_{\gamma} + \sigma_{B2} * f_{B2} + \sigma_{ppt} \quad [5.10]$$

Therefore, σ_{PD3-A} is calculated from Equation 15 to be 975 MPa, which is 40 MPa lower than the experimental yield strength of 1015 MPa. The major contribution to yield strength comes from solid solution strengthening of the matrix followed by strengthening from the second phase because of additional fine-size B2 platelets, and dislocation strengthening of the matrix. The overall yield strength of PD3-A is lower than that of PD3 due to annihilation defects. The contribution of various strengthening mechanisms to the overall yield strength of PD3-A is given in Table 5.8.

Contribution of various strengthening mechanisms to the yield strength of PD3-AB$_{30}$:

The yield strength of the austenite phase ($\sigma_{\gamma PD3-AB30}$) of PD3-AB$_{30}$ (100% austenite) is calculated using Equations 5.1-5.5 and the value is found to be 949 MPa.

The yield strength of coarse-sized banded and globular B2($\sigma_{B2PD1-B}$) for PD3-AB$_{30}$ (100% B2) is estimated using Equations 5.1-5.2, 5.4-5.6, and the value was found to be 1391 MPa.

To get the yield strength of PD3-AB$_{30}$, Equation 5.10 is modified as Equation 5.11.

$$\sigma_{PD3-AB30} = \sigma_{\gamma PD3-AB30} * f_{\gamma PD3-AB30} + \sigma_{B2PD3-AB30} * f_{B2PD3-AB30} + \sigma_{k-pearlite} + \sigma_{B2}$$

[5.11]

The total strength contribution from austenite and B2 is calculated to be 971 MPa, whereas the experimental yield strength is 1224 MPa. The difference between the experimental value and the calculated value is determined to be the strengthening from k-pearlite i.e., which is approximately 253 MPa.

If we consider the volume fraction of k-pearlite as 0.08, the estimated yield strength of k-pearlite is 3162 MPa.

The contribution of various strengthening mechanisms to the overall yield strength of PD3-AB_{30} is given in Table 5.8. The major contribution to the yield strength of PD3-AB_{30} comes from the solid solution strengthening of the matrix followed by strengthening from the second phase (elongated, globular, and platelets of B2, additional κ-pearlite and dislocation strengthening of the matrix. As a result, yield of PD3-AB_{30} is much higher than that of both PD3-A and PD3. The graphical representation of various strengthening mechanisms is also given in Figure 5.11.

Table 5.8: Contribution of different strengthening mechanisms to yield strength.

Material	PD3		PD3-A		PD3-AB_{30}	
Phase	Austenite	B2	Austenite	B2	Austenite	B2
Contribution to yield strength	(MPa)	(MPa)	(MPa)	(MPa)	(MPa)	(MPa)
σ_P	42	53	42	53	42	53
σ_{ss}	506	823	549	832	524	832
σ_{dis}	390	550	232	404	265	407
σ_{gb}	122	99	118	99	118	99
σ_{ppt} (platelet)	--		23		28	
σ_{ppt} (k-pearlite)	--		--		253	

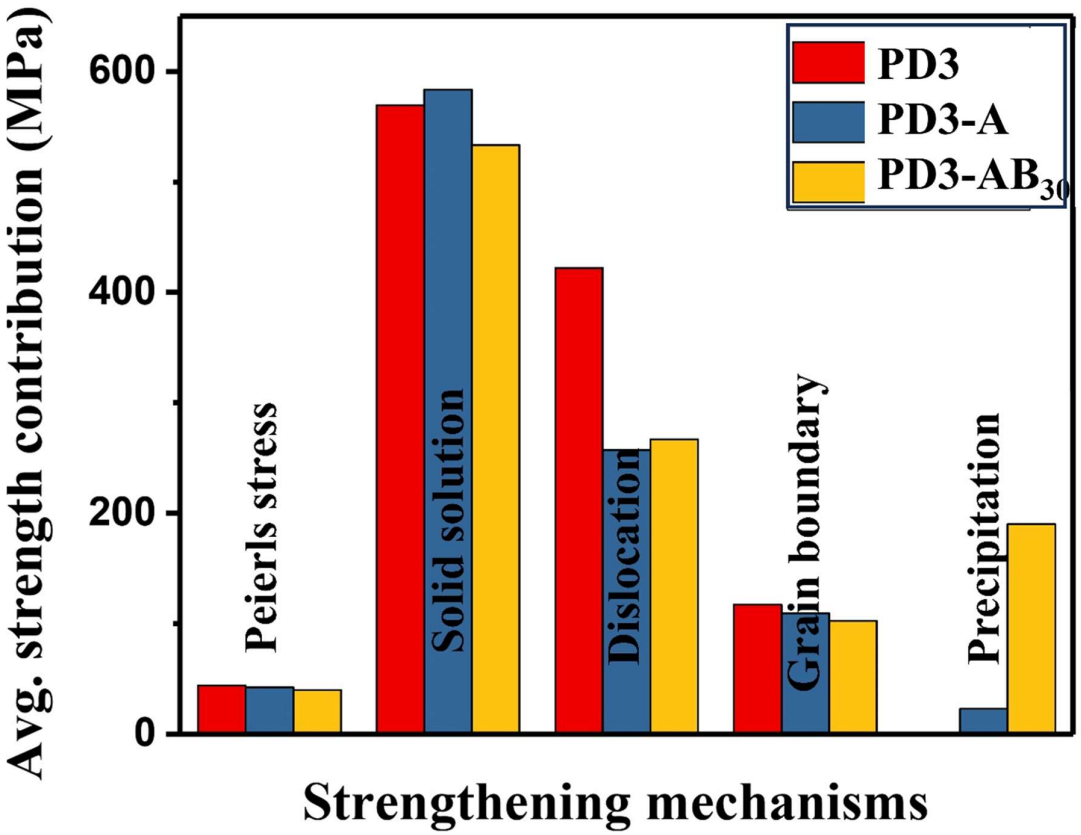

Figure 5.11: Strengthening mechanisms responsible for strength contribution to yield strength.

A higher dislocation density generally results in increased strength due to the resistance offered to dislocation motion. Comparing the annealed sample to the hot rolled and water-quenched sample, it is evident that the latter possesses a higher dislocation density, leading to a higher yield strength. Strengthening by dislocation is dominating over incoherent precipitation. As a result, annealed steel is softened. In the case of aged samples, the increase in yield strength is primarily attributed to the strengthening effect caused by the precipitation of kappa carbides in the form of k-pearlite. These precipitates act as obstacles to dislocation motion, thereby increasing strength.

5.3.2.2 Work hardening behavior

Differentiation of Ludwigson's equation concerning strain is given by Equation 5.12 which provides the changes in work hardening rate.

$$\frac{d\sigma}{d\varepsilon} = n_1 \exp(K_1 + n_1\varepsilon) + Kn\varepsilon^{n-1} \quad [5.12]$$

Equation 5.12 clearly states that there are two changes in the work hardening rate concerning true plastic strain. The significant initial work hardening observed in PD3-A can be attributed to the presence of fine non-shearable B2 platelets [145]. The work hardening rate decreases rapidly in stage I with the gradients of -59 GPa, -128 GPa, and -181 GPa for PD3, PD3-A, and PD3-AB_{30}, respectively. Stage 1 typically occurs as a result of the planar flow of dislocations over relatively long distances, wherein the dislocations encounter minimal obstacles, such as precipitates or grain boundaries, that hinder their movement [146]. Stage I is commonly referred to as the easy glide stage. This stage is observed within the strain range of 0.0-0.05 for PD3, 0.0-0.054 for PD3-A, and 0.0-0.061 for PD3-AB_{30}. In stage I the higher decreasing work hardening rate in PD3-AB_{30} than that of PD3-A and PD3 is due to rapid work hardening because of the combined effect of both B2 and k-pearlite. The initial work hardening rate at the easy glide stage increases with the increasing volume fraction of the second phase but decreases with decreasing size of precipitates. As a result, the work hardening rate of PD3-AB_{30} is higher than that of PD3-A and PD3 but the higher decrease in work hardening rate with increasing strain in PD3-AB_{30} than that PD3-A and PD3 is due to strengthening from extra fine B2 platelets and κ-pearlite.

In stage II, the rate of work hardening decreases gradually within the range of 0.05-0.127, and 0.054-0.137 plastic strain for PD3 and PD3-A, respectively. However, a slight increase in the work hardening rate is observed for PD3-AB_{30} in the strain range of 0.061-0.101. In Stage II, the activation of cross-slip and multiple-slip systems facilitates the formation of

heterogeneous dislocation structures [125]. This stage corresponds to enhanced dislocation storage, as suggested by the proliferation of walls and cell structures. Consequently, there is an increase in dislocation density. The work hardening rate decreases with a gradient of -4 GPa in PD3, -6 GPa in PD3-A, and an observed increase in a gradient of 4 GPa in PD3-AB30. A slight increase in the work hardening rate in PD3-AB_{30} is caused by the presence of short-range ordered structures (K-pearlite) [147], however, the material fails at an early true plastic strain of 0.1.

The stage III (Figure 5.8(b)) of the linear relationship between the hardening rate ($\frac{d\sigma}{d\epsilon_p}$) versus true stress ($\sigma$) can be best explained by the Kock, Mecking [118] model, which is shown in Equation 5.13 as:

$$n3 = \frac{d\sigma}{d\epsilon_p} = \theta_0 + m\sigma \quad [5.13]$$

In this equation, $n3$ and σ represent the strain hardening rate, and the true flow stress, respectively. The constant θ_0 is related to the dislocation storage term which is equal to the work hardening rate and is determined from the slope of true stress vs true strain of stage II. The second term is associated with dynamic recovery. The term m pertains to the slope of the linear regimes associated with the annihilation of dislocations due to cross slip during dynamic recovery. A high value of θ_0 indicates a high dislocation storage capacity, while a high magnitude of m indicates high dynamic recovery [127]. Figure 5.12 gives the plot of the work-hardening rate ($\frac{d\sigma}{d\epsilon_p}$) vs plastic stress for PD3 and PD3-A. Equation 12 is plotted using data from Figure 5.8 (b) The results of the linear fitting for the third stage of both PD3 and PD3-A samples are illustrated in Figure 5.12. PD3-AB_{30} fails at low strain much before reaching stage III. Limited ductility reduces activities of dislocation and avoids dynamic recovery in PD3-AB_{30}.

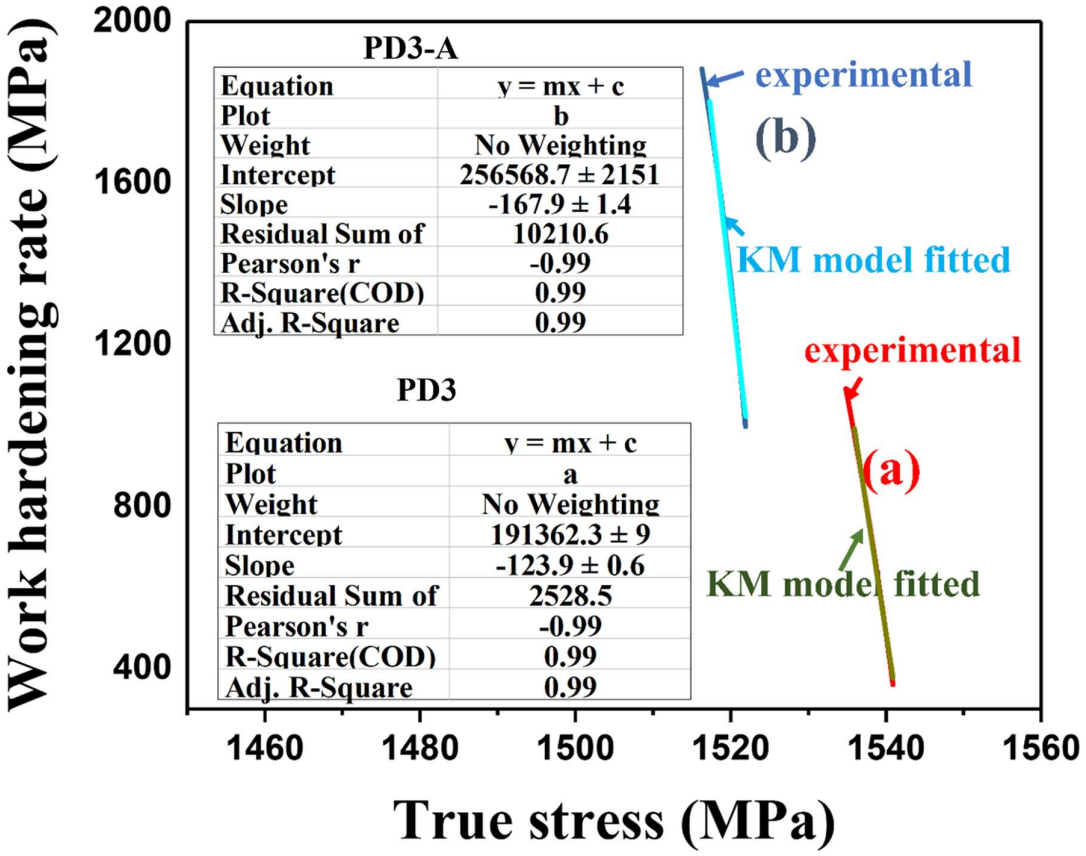

Figure 5.12: Experimental work hardening rate vs true stress in stage III and fitted curve as per KM model (Equation 5.13) for (a) PD3 and (b) PD3-A.

The Adjusted R^2 value of the fitted curve is nearly 1, which indicates a very high correlation between the experimental data and the fitted curve. The dislocation storage capacity (θ_0) of PD3 and PD3-A are found to be 4570 MPa and 8260 MPa, respectively. This suggests that PD3-A has a higher dislocation storage capacity compared to PD3. On the other hand, the negative slope (m) of the curve for PD3 and PD3-A are found to be -123.9 and -167.9, respectively. This suggests that PD3-A has a higher dynamic recovery compared to PD3. The decrease in plastic elongation of PD3-A and PD3-AB_{30} compared to PD3 is due to the formation of brittle phases like extra B2 platelets in PD3-A and k-pearlite in PD3-AB_{30} which result in a reduction in the area percentages and the average sizes of dimples as the conditions change from hot rolling to annealing and finally aging. The observed fracture

mode in all materials can be categorized as mixed mode, i.e. ductile-brittle mode of fracture.

Coarse size and low volume fraction of B2 precipitate result in a low work hardening rate in PD3 which leads to a minimum hardening of 158 MPa that provides a low ultimate tensile strength of 1296 MPa. The higher volume fraction and uniform distribution of B2 precipitate in PD3-A provide higher work hardening in combination with high plastic elongation providing to maximum increase in strength of 239 MPa to achieve a high ultimate tensile strength of 1254 MPa. Non-uniform distribution of lamellar k-pearlite restricts plastic elongation of 9% in PD3-AB_{30}. In PD3-AB_{30}, a higher work hardening rate than that of PD3 and PD3-A, but restricted plastic elongation of 9% results in lower hardening of 209 MPa. As yield strength is higher even lower amount of work hardening provides maximum ultimate tensile strength of 1430 MPa.

5.3.3 Comparison of tensile properties with automotive steels

A comparison is presented between the yield strength (Figure. 5.13(a)), and ultimate tensile strength (Figure 5.13(b)), concerning the elongation of conventional automotive steels [6] and the current steels under different processing conditions in Figure 5.13. The yield strength, tensile strength, total elongation, specific yield strength, and specific tensile strength of currently developed PD3-A low-density steels are superior to Mart 950/1200, CP700/800, and DP700/1000 steels (Table 5.9). The material PD3-AB_{30} displays comparable mechanical properties to that of MnB 1200/1600 and Mart 1250/1520 steels (Table 5.9).

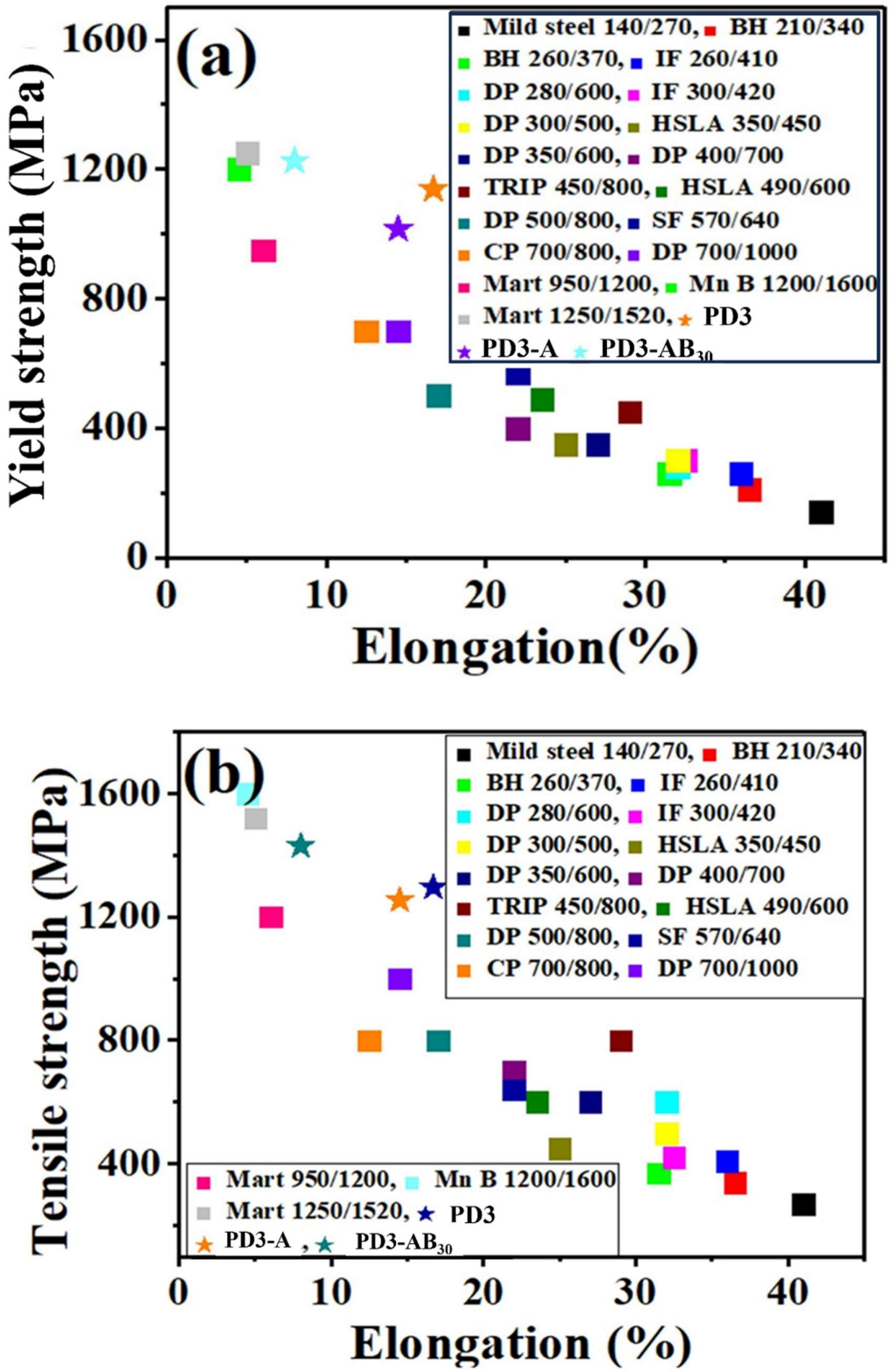

Figure 5.13: Tensile properties of automotive steels (a) yield strength vs elongation and (b) tensile strength vs elongation. Corresponding properties of experimental steels are superimposed [6].

Table 5.9: Comparison of Tensile properties of a few commercial steels to newly developed low-density steels.

Material	YS (MPa)	UTS (MPa)	Total elongation, %	Specific YS (MPa.cc/g)	Specific UTS(MPa.cc/g)	Ref.
Mart 950/1200	950	1200	6	121.8	153	[6]
CP 700/800	700	800	12.5	89.7	102.6	[6]
DP 700/1000	700	1000	14.5	89.7	128.2	[6]
Mn B 1200/1600	1200	1600	4.5	153.8	205.1	[6]
Mart 1250/1520	1250	1520	5	160.25	194.9	[6]
PD3-A	1015	1254	16.3	152.2	188	Present work
PD3-AB_{30}	1224	1430	10.3	209.6	223.8	Present work

Tensile toughness can be represented by the product of strength and elongation (PSE). The total elongations of Mart 950/1200, DP 700/1000, CP 700/800, Mn B 1200/1600, and Mart 1250/1520 steel grades are 6%, 14.5%, 12.5%,4.5 %, and 5% respectively and respective PSE values are 7.2 GPa%, 14.5 GPa%, 10.0 GPa%, 6.3 GPa%, and 6.93 GPa%. The PSE values for PD3-A and PD3-AB_{30} steels are calculated to be 17.8 GPa% and 16.0 GPa%, respectively. Mart 950/1200 grade steel, is commonly used in the production of cross-members, side intrusion beams, bumper beams, and bumper reinforcements due to high

energy absorption during crashes. If Mart 950/1200 grade steel is replaced with PD3-A, the material thickness can be reduced by 59.5% due to toughness consideration, i.e. 59.5% reduction in weight, however, the reduction in thickness cannot be solely based on an increase in PSE (Product of Strength and Elongation) if other factors like the geometry of the part, the mode of loading, and how the material behaves under different stress conditions are varied. Considering the respective density of martensitic steel and annealed low-density steel, as 7.8 g/cc and 6.67 g/cc, additionally, an extra 5.8 % reduction in weight can be achieved because of decreased density. Therefore, the replacement of Mart 950/1200 steel with annealed low-density steel (PD3-A) may potentially bring a weight reduction of 65.3% if implemented successfully, provided their formability is optimized for complex geometries and appropriate coatings are developed to ensure corrosion resistance and surface protection.

5.4 Conclusions

The following conclusions can be drawn based on the microstructure and tensile properties of a hot rolled and aged duplex low-density steel.

- The incorporation of 10.5 mass % aluminum in the selected steel has resulted in a significant reduction in density, almost 14 % compared to the density of conventional ferritic steels. The density of the current steel is measured to be 6.67 g/cc.
- Homogenization and hot rolling of the selected low-density steel (PD3) produces a two-phase microstructure of austenite and 13% B2 with a significant amount of dislocation density. Hot rolling followed by rapid quenching in water prevents the precipitation of kappa carbide. Strengthening of PD3 is dominated by solid

solution, followed by dislocations, grain boundary, and friction strengthening in decreasing order, reaching a yield strength of 1138 MPa.

- Annealing of PD3 at 930°C for 30 min (PD3-A), softens both austenite and B2 by reducing respective dislocation densities with additional precipitation of 5 % B2 platelets. The additional precipitation is unable to compensate for the loss due to softening from a reduction in dislocation density. As a result, the strengthening of PD3-A is also dominated by solid solution, followed by dislocations, grain boundary, and friction in decreasing order, reaching a reduced yield strength of 1015 MPa compared to PD3.
- Ageing of PD3-A at 550°C for 30 min (PD3-AB_{30}) results in precipitation of kappa carbides and ferrite in pearlite form, which contributes an additional significant amount of strengthening of 253 MPa in yield strength. As a result, PD3-AB_{30} exhibited the highest yield strength of 1224 MPa.
- PD3 reports highest ductility of 16.7%. Ductility decreases to 14.5% due to precipitation of B2 platelets in PD3-A. Ductility reduces further to 9.3% due to the formation of K-pearlite near the grain boundary in PD3-AB_{30}. Selected low-density steels fail by mixed mode of ductile-brittle fracture.
- PD3 and PD3-A as well as PD3-AB_{30} follow Ludwigson flow behavior of two stages i.e. easy glide followed by steady-state work hardening. Work hardening rate increases with increasing volume fraction but decreasing size of precipitates. As a result, the work hardening rate of PD3-AB_{30} is maximum in the easy glide stage, however, limited ductility reduces activities of dislocation and avoids dynamic recovery in PD3-AB_{30}.
- Coarse size and low volume fraction of B2 precipitate result in a low work hardening rate in PD3 which leads to a minimum hardening of 158 MPa that

provides a low ultimate tensile strength of 1296 MPa. The higher volume fraction and uniform distribution of B2 precipitate in PD3-A lead to a maximum amount of work hardening of 239 MPa which helps to achieve a high ultimate tensile strength of 1254 MPa. Non-uniform distribution of lamellar k-pearlite restricts plastic elongation of 9% in PD3-AB_{30}, which results in a lower amount of work hardening of 206 MPa but the material displays maximum ultimate tensile strength of 1430 MPa due to high yield strength.